RESEARCH ARTICLE

Functional Reprogramming of Neutrophils within the Brain Tumor Microenvironment by Hypoxia-Driven Histone Lactylation

Alessio Ugolini[1,2,3], Alessandra De Leo[1,2], Xiaoqing Yu[4], Fabio Scirocchi[1,3,5], Xiaoxian Liu[4], Barbara Peixoto[1,2], Delia Scocozza[1], Angelica Pace[3], Michela Perego[2], Alessandro Gardini[2], Luca D'Angelo[6], James K.C. Liu[7], Arnold B. Etame[7], Aurelia Rughetti[3], Marianna Nuti[3], Antonio Santoro[6], Michael A. Vogelbaum[7], Jose R. Conejo-Garcia[8], Paulo C. Rodriguez[1], and Filippo Veglia[1,2,7]

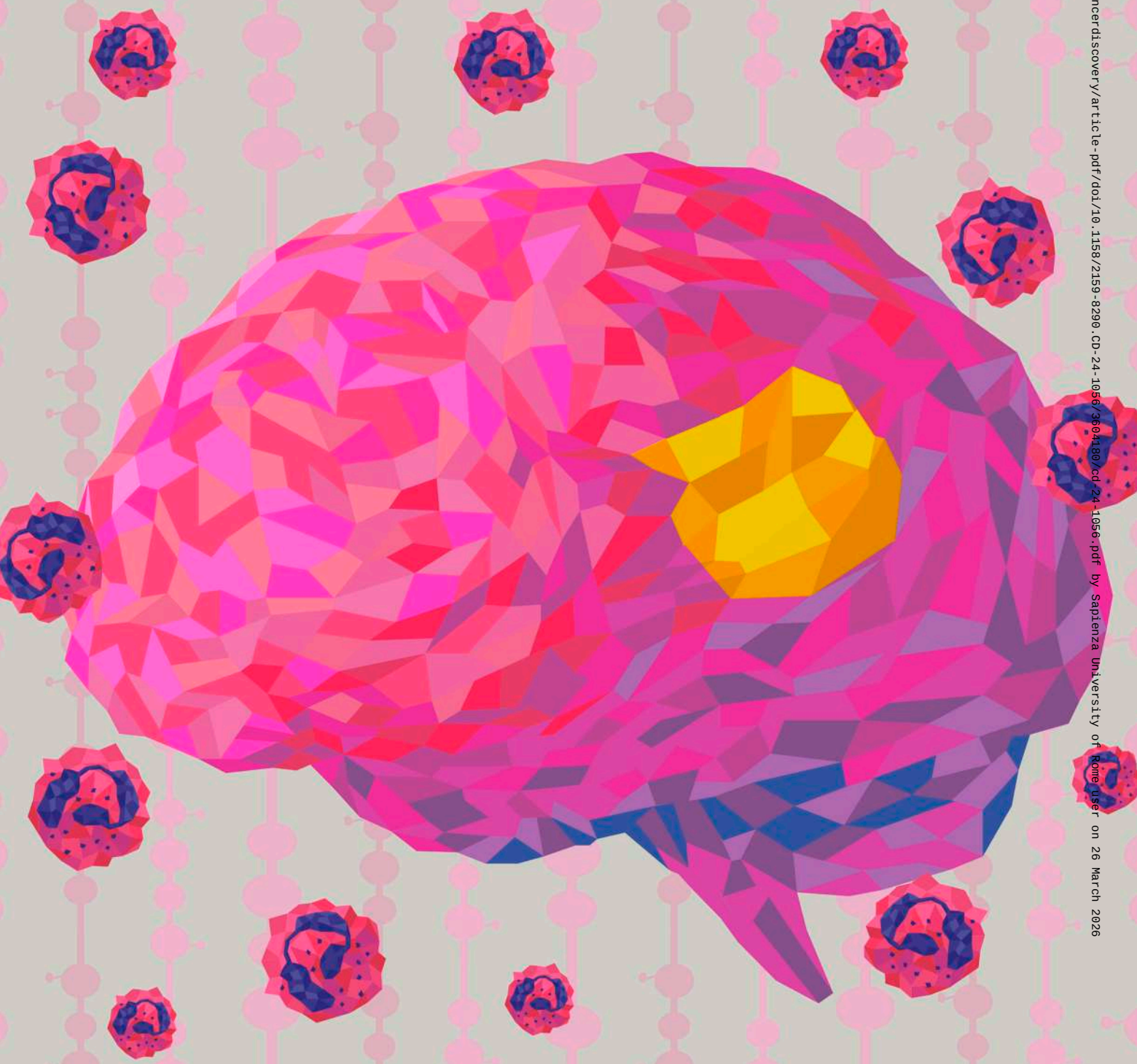

ABSTRACT Despite functional heterogeneity, the high frequency of intratumoral neutrophils predicts poor clinical outcomes. The tumor microenvironment reprograms neutrophils into immunosuppressive subsets that hinder anticancer immunity, thereby contributing to tumor growth and resistance to immunotherapies. However, the mechanisms underlying neutrophil reprogramming remain elusive. In this study, we report that the immunosuppressive ability of brain tumor–infiltrating neutrophils was restricted to a highly glycolytic and long-lived subset expressing CD71, which acquired immunosuppressive properties in response to hypoxia. Mechanistically, hypoxia boosted glucose metabolism in CD71$^+$ neutrophils, leading to high lactate production. Lactate caused histone lactylation, which subsequently regulated arginase-1 expression, required for T-cell suppression. Targeting histone lactylation with the antiepileptic drug isosafrole blocked CD71$^+$ neutrophil immunosuppressive ability, delayed tumor progression, and sensitized brain tumors to immunotherapy. A distinctive gene signature characterizing immunosuppressive CD71$^+$ neutrophils correlated with adverse clinical outcomes across diverse human malignancies. This study identifies histone lactylation as a potential therapeutic target to counteract neutrophil-induced immunosuppression within tumors.

SIGNIFICANCE: Neutrophils are critical contributors to the immunosuppressive microenvironment that restricts the effects of promising immunotherapies in glioblastoma. Our study identifies hypoxia-driven histone lactylation as a potential target to block immunosuppressive neutrophils and boost the effects of immunotherapy in glioblastoma and in other cancer settings beyond brain tumors.

INTRODUCTION

Neutrophils are released into circulation mainly from the bone marrow (BM) and abundantly infiltrate tumors. Neutrophils have emerged as important regulators of immune responses within the tumor microenvironment (TME; refs. 1–3). Traditionally, although the antitumoral functions of neutrophils have been reported, particularly during early tumorigenesis, they acquire potent protumoral and immunosuppressive properties at later stages of tumor progression. A high abundance of neutrophils in tumor tissue is a predictor of poor prognosis in different cancers, including glioblastoma (GBM; ref. 4), which is the most aggressive and lethal primary brain tumor with high resistance to immunotherapies (5, 6).

Distinct populations of neutrophils coexist in the same TME (7–11). Tumor-infiltrating neutrophils, which significantly differ from peripheral neutrophils (7, 12), acquire protumoral properties, thereby reflecting functional reprogramming within tumor tissue. In response to local TME cues, neutrophils undergo profound metabolic adaptation, which is instrumental for the acquisition of specific functions within tumors (13). A major consequence of this metabolic reprogramming is the acquisition of the ability to suppress the activity of other immune cells, particularly T cells (14). However, the characterization of the metabolic drivers of the reprogramming of tumor-infiltrating neutrophils into immunosuppressive cells remains elusive.

Protumoral neutrophils with hyperactivated glycolysis are found in the pancreatic TME and are localized in hypoxic/glycolytic areas of tumors, in which they exert proangiogenic functions to support tumor growth (10, 11). Glucose metabolism promotes the immunosuppressive activity of monocyte-derived macrophages (MDM), and GLUT1-deficient neutrophils are unable to exert their immunosuppressive function in GBM tumors (15), suggesting that glucose may play a role in the acquisition of protumoral functions in the TME. Glucose is critical for allowing neutrophils to respond to pathogens, but whether glucose metabolism may reprogram neutrophils into immunosuppressive cells within the TME is unknown. Dissecting these mechanisms may lead to the development of strategies aimed at reprogramming the function of immunosuppressive neutrophils for cancer therapy.

In this study, we found that hypoxia-driven glucose metabolism reprogrammed the immunosuppressive function of a specific subset of neutrophils expressing CD71 via histone

[1]Department of Immunology, H. Lee Moffitt Cancer Center, Tampa, Florida. [2]Immunology, Genome Regulation and Cell Signaling Program, The Wistar Institute, Philadelphia, Pennsylvania. [3]Department of Experimental Medicine, Sapienza University of Rome, Rome, Italy. [4]Department of Biostatistics and Bioinformatic, H. Lee Moffitt Cancer Center, Tampa, Florida. [5]Department of Onco-Hematology, Gene and Cell Therapy, Bambino Gesù Children's Hospital–IRCCS, Rome, Italy. [6]Department of Human Neurosciences, Neurosurgery Division, "Sapienza" University, AOU Policlinico Umberto I, Rome, Italy. [7]Department of Neuro-Oncology, H. Lee Moffitt Cancer Center, Tampa, Florida. [8]Department of Integrative Immunobiology, Duke School of Medicine, Durham, North Carolina.

Corresponding Author: Filippo Veglia, The Wistar Institute, 3601 Spruce Street, Philadelphia, PA 19104. E-mail: fveglia@wistar.org

Cancer Discov 2025;XX:1–27

doi: 10.1158/2159-8290.CD-24-1056

lactylation, which directly regulated the expression of ARG1 in these cells. The signature of immunosuppressive and glycolytic CD71$^+$ neutrophils was associated with poor outcomes across several human cancers. These results suggest the opportunity to target immunosuppressive neutrophils in brain tumors and other malignancies.

RESULTS

Neutrophils with Immunosuppressive Activity Infiltrate Murine and Human Brain Tumors

To examine the role of neutrophils in brain cancer, we first analyzed the abundance of neutrophils in brain tumor tissues in different orthotopic models of brain tumors (GL261 and SB28) by flow cytometry (FACS). Using the gating strategy shown in Fig. 1A, we found that the frequency of neutrophils was higher in the spleen and blood, but not in the BM, of both brain tumor models compared with naïve mice injected with vehicle (Supplementary Fig. S1A). A robust infiltration of neutrophils was observed in the brain tumor beds of the SB28 model, compared with GL261 and naïve mice (Fig. 1B). We then analyzed the kinetics of neutrophil accumulation in brain tumor tissue and blood during SB28 tumor growth. We found that neutrophils mostly accumulated in blood and tumors at late stages of malignant progression (Fig. 1C), which correlated with an increased tumor size (Supplementary Fig. S1B). However, at earlier time points, the frequency of neutrophils in blood and tissue was similar to that observed in naïve mice (day 0). On the other hand, even if the GL261 model displayed an expansion of neutrophils in the circulation at later stages, their accumulation in the brain was only slightly increased during tumor progression (Fig. 1D). Of note, SB28 brain tumors recapitulate key characteristics of human GBM, such as aggressive growth and resistance to immunotherapy (16), compared with GL261.

Considering the abundance of neutrophils in SB28 tumors, we next sought to determine whether neutrophils contribute to brain tumor growth. To this end, we depleted neutrophils in mice with brain tumors (SB28) using an optimized approach for durable neutrophil depletion (Supplementary Fig. S1C; ref. 17). Neutrophil depletion was effective in both the blood and tumor tissue (Fig. 1E; Supplementary Fig. S1D and S1E) at the endpoint and correlated with enhanced survival of mice with brain tumors (Fig. 1E). Next, we analyzed the brain tumor immune landscape upon neutrophil depletion by FACS (Supplementary Fig. S1F). To reduce the possibility that changes in immune cell populations could potentially be attributed to variations in tumor size, we analyzed immune cells at day 14 (Supplementary Fig. S1C) when some mice started showing neurologic symptoms as a result of an advanced tumor. Intratumoral neutrophil depletion (Fig. 1F; Supplementary Fig. S1G) was associated with an increased frequency and absolute numbers of CD4$^+$ and CD8$^+$ T cells (Fig. 1F and G). Although we found an increase in the absolute numbers of microglia (MG) and NK T cells upon neutrophil depletion, no changes in the frequency and absolute numbers of MDM, monocytes, and different subsets of dendritic cells (cDC1, cDC2, LY6C$^+$ DC), as well as NK cells (Fig. 1F; Supplementary Fig. S1G), were observed. These results suggest that tumor-associated neutrophils may have an independent protumoral role in brain tumors.

As the depletion of neutrophils correlated with higher T-cell accumulation in brain tumors, we asked whether neutrophils display immunosuppressive activity in GBM. Thus, FACS-sorted neutrophils (CD45$^+$CD11b$^+$Ly6G^{high}LY6C$^{lo/-}$F4/80$^{lo/-}$) from BM, spleen, and brain tumors were cocultured with autologous anti-CD3–/anti-CD28–primed CD3$^+$ T cells, prestained with carboxyfluorescein diacetate succinimidyl ester (CFSE). Contrary to BM and spleen neutrophils, which lacked suppressive ability, intratumoral neutrophils restricted CD8$^+$ and CD4$^+$ T-cell proliferation (Fig. 1H). The acquisition of suppressive activity in tumor beds correlated with high expression of arginase-1 (*Arg1*), nitric oxide synthase 2, NADPH oxidase 2, and programmed death-ligand 1 compared with BM and spleen neutrophils (Supplementary Fig. S1H). Together, these data indicate that neutrophils acquired immunosuppressive activity in the TME but not in peripheral organs/tissues.

To confirm the relevance of these findings, we analyzed the frequency of neutrophils in freshly dissociated human brain tumors. Using the gating strategy in Fig. 1I, we observed that neutrophils (CD45$^+$CD66b$^+$CD14$^-$) infiltrated human brain tumors, in which they represented 15% to 20% of total CD45$^+$ cells (Fig. 1I). Neutrophils had a slight but not significant tendency to accumulate more in GBM tumors compared with oligodendrogliomas and astrocytomas (Fig. 1J). Newly diagnosed and recurrent brain tumors (Supplementary Fig. S1I) showed similar frequencies of neutrophils. Correlation analysis using The Cancer Genome Atlas (TCGA) GBM datasets revealed that higher CD15 expression (a neutrophil marker) correlated with worse clinical outcomes in patients with GBM (Fig. 1K). Next, to examine neutrophils' immunosuppressive activity, we co-cultured FACS-sorted neutrophils from the blood or tumors of patients with brain cancer with autologous T cells, prestained with CFSE, and stimulated with anti-CD3/anti-CD28 antibodies. As found in mouse models, tumor-infiltrating neutrophils suppressed CD4$^+$ and CD8$^+$ T-cell proliferation compared with blood-derived neutrophils, which lacked suppressive properties (Fig. 1L). The acquisition of immunosuppressive activity was accompanied by higher expression of LOX1 (Supplementary Fig. S1J), a surface marker used to identify immunosuppressive neutrophils (18). Importantly, the high density of neutrophils in brain cancer tissues inversely correlated with the infiltration of CD3$^+$, CD8$^+$, and CD4$^+$ T cells (Fig. 1M).

Collectively, our data indicate that neutrophils abundantly accumulate in the periphery and brain tumors but acquire potent immunosuppressive activity preferentially in the brain TME, suggesting that local brain tumor cues drive the functional reprogramming of neutrophils that ultimately support tumor growth.

CD71 Identifies a Subset of Glycolytic Neutrophils That Is Preferentially Distributed in Hypoxic/Glycolytic Niches

Given the functional and phenotypic heterogeneity of neutrophils in cancer (2), we employed single-cell RNA sequencing (scRNA-seq) to identify potential neutrophil subsets with

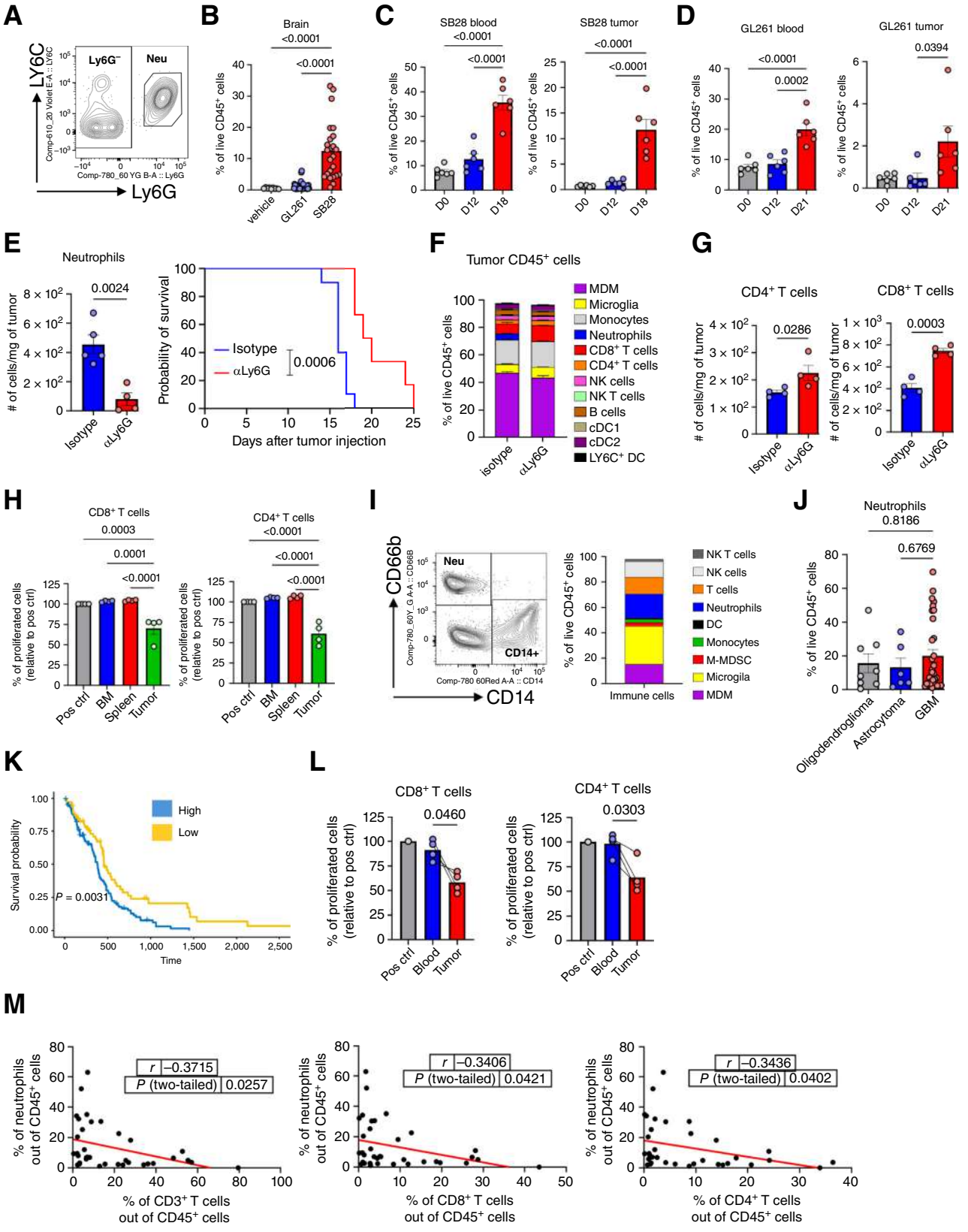

Figure 1. Neutrophils infiltrate brain tumors, acquiring immunosuppressive features. **A,** Example of murine brain tumor–derived neutrophils gating strategy by FACS on live CD45⁺ CD11b⁺ F4/80$^{lo/-}$cells. **B,** Frequency of neutrophils out of live CD45⁺ cells in the brain of vehicle (RPMI) versus GBM-bearing mice by FACS. Vehicle $n = 9$, GL261 $n = 35$, SB28 $n = 24$ mice. **C,** Frequency of neutrophils out of live CD45⁺ cells in SB28-bearing (*continued on following page*)

immunosuppressive activity. Toward this goal, we FACS-sorted neutrophils from the blood and tumors of mice with brain tumors (SB28) at a late stage (day 18) and processed them for scRNA-seq using the 10× Genomics Chromium platform (Fig. 2A).

Unbiased, graph-based clustering identified two main neutrophil clusters (N1 and N2) in blood and three clusters (N1, N2, and N3) in brain tumor tissue (Fig. 2B). N1, N2, and N3 demonstrated distinct gene expression profiles (Fig. 2C; Supplementary Fig. S2A). Although N1 was the main cluster in circulation, it represented a small proportion of neutrophils in brain tumors. The proportion of cluster N2 was much higher in brain tumors compared with blood. Cluster N3 was instead almost exclusively found in brain tumors (Fig. 2B).

To obtain a more granular characterization of neutrophil clusters, we ran gene set enrichment analysis (GSEA) in combined blood and tumor clusters. We found that the hypoxic and glycolytic pathways were the most significantly enriched pathways in N3 compared with the other clusters (Fig. 2D; Supplementary Fig. S2B and S2C). The N1 and N2 clusters showed higher enrichment in pathways related to proinflammatory and immune responses, reactive oxygen species, as well as type 1 and 2 IFN responses (Fig. 2D; Supplementary Fig. S2B and S2C).

Next, we searched for highly expressed transmembrane receptors in our list of the top 30 differentially expressed genes (DEG; Fig. 2C) that could potentially allow the identification and characterization of putative N3 neutrophils. We found that the transferrin receptor CD71 (encoded by the *Tfrc* gene) was largely expressed by N3 (Fig. 2E). Additionally, the highest expression of *Tfrc* correlated with the highest enrichment in glycolysis and hypoxia, as well as the highest expression of lactate dehydrogenase A (*Ldha*) and *Glut1* (encoded by *Slc2a1*) observed in N3 (Fig. 2E), indicating that N3 is probably a population of highly glycolytic and hypoxic neutrophils expressing CD71. As we recently found that GLUT1-deficient neutrophils lacked their suppressive ability in brain tumors (15) and the N3 cluster is similar to a neutrophil subset (T3) with protumoral functions identified in pancreatic tumors (Supplementary Fig. S2D; ref. 10), our data suggest that the N3 cluster may have immunosuppressive activity in brain tumors.

To validate our results, we analyzed the expression of CD71 in neutrophils from brain tumor–bearing mice by FACS. Brain tumor–infiltrating neutrophils expressed higher CD71 levels compared with neutrophils from other peripheral organs/tissues of the same mice with brain tumors by both qRT-PCR and FACS (Supplementary Fig. S2E). Based on CD71 expression, we identified two main subsets of neutrophils in brain tumors: $CD71^-$ and $CD71^+$ neutrophils (Fig. 3A). $CD71^+$ neutrophils represented about 25% to 30% of total neutrophils that infiltrated SB28 tumors, in contrast to 6% to 7% in BM and blood. They were almost undetectable in the spleen (Fig. 3A). However, the proportion of $CD71^+$ neutrophils in total neutrophils was similar between BM and spleen of brain tumor–bearing and naïve mice. $CD71^+$ neutrophils accumulated in blood and tumors at late stages of tumor growth, compared with naïve blood (D0) and brain tissue (D0), respectively (Fig. 3B). This is in line with the increased total neutrophil accumulation in blood and tumors (Fig. 1C). Furthermore, by using bulk RNA-seq on $CD71^+$ and $CD71^-$ neutrophils FACS-sorted from SB28 brain tumors, we found 3,494 DEGs, of which 2,322 were upregulated ($\log_2$ fold change (FC) > 1 and adjusted $P < 0.05$) and 1,172 were downregulated ($\log_2$FC < −1 and adjusted $P < 0.05$) in $CD71^+$ neutrophils compared with $CD71^-$ neutrophils from mouse brain tumors (Fig. 3C). Our data suggest that $CD71^+$ and $CD71^-$ neutrophils expand during tumor progression and are transcriptionally distinct subsets in the brain tumor TME.

GSEA of the bulk RNA-seq confirmed the enrichment in glycolysis and angiogenesis in $CD71^+$ neutrophils, compared with $CD71^-$ neutrophils (Supplementary Fig. S2F). Therefore, we sought to determine whether $CD71^+$ neutrophils are glycolytic cells within brain tumors. Thus, we analyzed their ability to uptake glucose by using the fluorescent glucose tracer 2-(N-(7-nitrobenz-2-oxa-1,3-diazol-4-yl)amino)-2-deoxyglucose by FACS (19). $CD71^+$ neutrophils showed higher avidity for glucose (Fig. 3D), which correlated with higher GLUT1 (Fig. 3E) and LDHA (Fig. 3F) expression and intracellular lactate accumulation, compared with $CD71^-$neutrophils (Fig. 3G). Consistently, $CD71^+$ neutrophils from brain tumors showed a higher expression of different glycolysis-associated genes (*Aldoc*, *Pkm*, and *Ldha*) by qRT-PCR (Supplementary Fig. S2G).

Considering that the N3 cluster showed enrichment in hypoxia and glycolysis, we sought to investigate whether $CD71^+$ neutrophils experience hypoxia in mouse brain tumors. Thus, we injected pimonidazole (PIMO), a hypoxia tracer, into SB28-bearing mice at terminal stages of malignant progression and performed anti-PIMO intracellular staining (20). By FACS, we found that both $CD71^-$ and $CD71^+$ neutrophils experienced

Figure 1. ***(Continued)*** mice ($n = 6$) by FACS in blood (left) versus tumor (right). **D,** Frequency of neutrophils out of live $CD45^+$ cells in GL261-bearing mice ($n = 6$) by FACS in blood (left) versus tumor (right). **E,** Absolute numbers of neutrophils per milligram of tumor in SB28-bearing mice at the endpoint ($n = 4$–5) by FACS (left) and Kaplan–Meier representation of SB28-bearing mice survival (right) after treatment with the isotype control ($n = 7$) or the neutrophil-depleting strategy ($n = 6$; αLy6G). **F,** Frequencies of different immune cell populations out of live $CD45^+$ cells in tumors of SB28-bearing mice at day 14 after neutrophil depletion by FACS ($n = 4$). **G,** Absolute numbers of $CD4^+$ (left) and $CD8^+$ (right) T cells per milligram of tumor in SB28-bearing mice at day 14, by FACS ($n = 4$). **H,** Suppressive ability of SB28-bearing mice–derived neutrophils on $CD8^+$ and $CD4^+$ T-cell proliferation, measured as CFSE dilution by FACS ($n = 4$). **I,** Example of human brain tumor–derived neutrophil gating strategy by FACS, on live $CD45^+$ cells (left) and frequencies of different immune cell populations out of live $CD45^+$ cells in patients with brain cancer from Moffitt Cancer Center (USA) and Policlinico Umberto I (Italy) by FACS (right, $n = 44$). **J,** Frequency of neutrophils out of live $CD45^+$ cells in patients with brain cancer divided based on the diagnosis from Moffitt Cancer Center and Policlinico Umberto I by FACS. Oligodendroglioma $n = 8$, astrocytoma $n = 6$, GBM $n = 30$. **K,** Survival analysis based on CD15 expression in the TCGA GBM dataset. Patients were divided into high and low groups based on the optimal cutoff. (**L**). Suppressive ability of human brain tumor–derived neutrophils on $CD8^+$ and $CD4^+$ T-cell proliferation, measured as CFSE dilution by FACS ($n = 4$). **M,** Correlation between the presence of neutrophils and T cells in the tumors of patients with brain cancer by FACS ($n = 25$). All data are presented as mean ± SEM. Statistical analysis was performed using one-way ANOVA with Tukey's *post hoc* test (**B**, **C**, **D**, **H** and **J**), the Kaplan–Meier method and log-rank test (**E**), unpaired two-sided Student *t* tests (**E** and **G**), paired two-sided Student *t* tests (**L**), and Pearson correlation coefficient with the associated two-tailed *P* value (**M**).

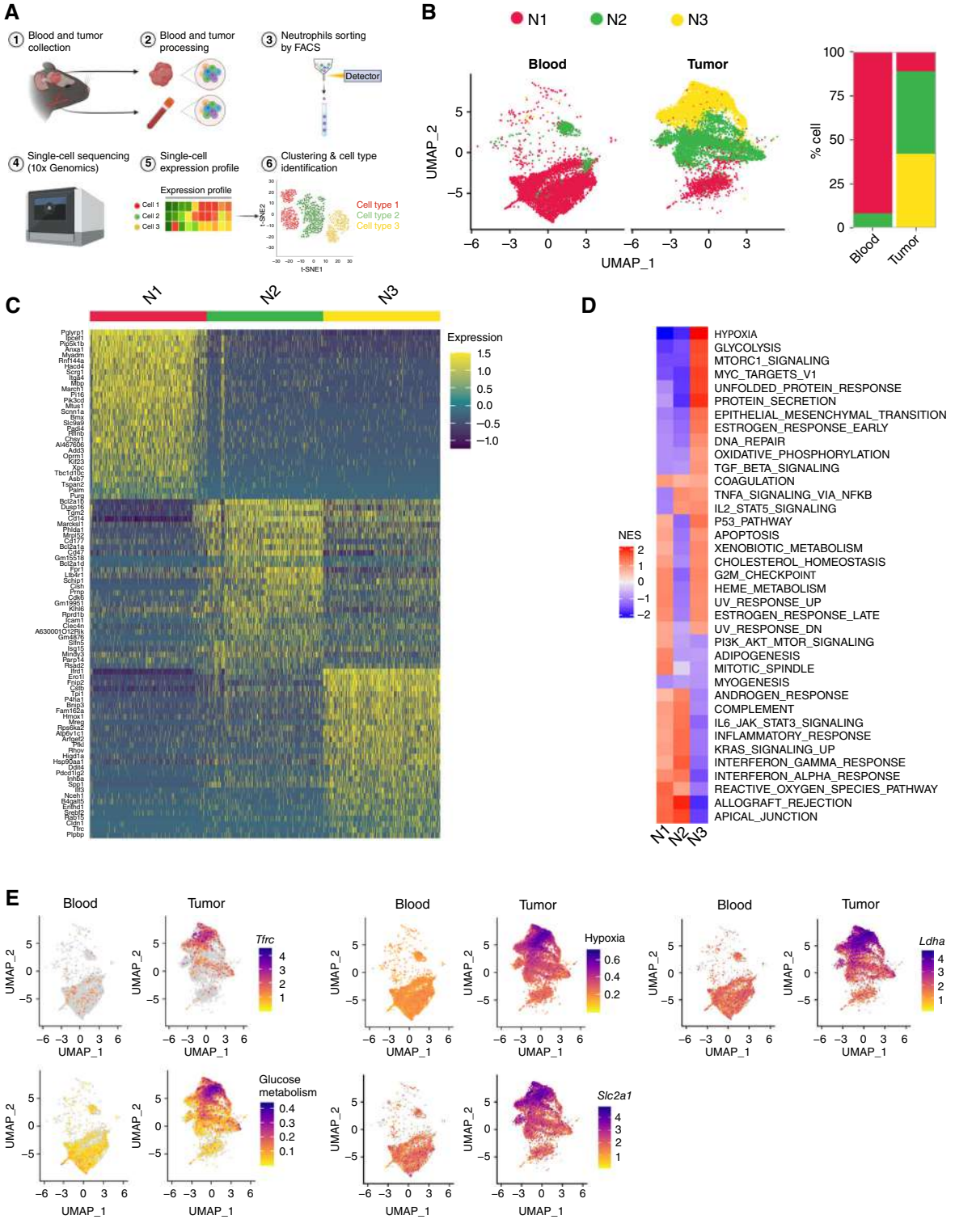

Figure 2. A population of glycolytic neutrophils expressing the CD71 receptor is expanded in brain tumors, in which it acquires a hypoxic signature. **A,** Schematic representation of the step-by-step process to isolate and sequence neutrophils from brain tumor–bearing mice for scRNA-seq with 10x Genomics. **B,** Uniform Manifold Approximation and Projection for Dimension Reduction (UMAP) projection of neutrophils with cells colored by clusters N1, N2, and N3 (left) and cluster composition in tumor versus blood samples (right). **C,** Heatmap of signature genes exclusively expressed in each neutrophil cluster. Shown are Z-scale gene expression levels. **D,** GSEA showing enriched Hallmark pathways in each neutrophil cluster, including both blood and tumor clusters. Shown are normalized enrichment scores. **E,** CD71 (*Tfrc*), LDHA (*Ldha*), GLUT1 (*Slc2a1*), glycolysis, and hypoxia expression on UMAP, separating blood from tumor clusters. Glycolysis and hypoxia overall expression were derived using the glucose metabolism gene set in REACTOME and the hypoxia gene set in the Hallmark database, respectively (**A,** Created with BioRender.com.)

a similar degree of hypoxia in GBM tumors compared with their counterparts in the spleen (Supplementary Fig. S3A). To better define the distribution of neutrophil subsets in mouse brain tumor tissues, we employed immunofluorescence. As recently shown (10), we defined hypoxic regions as CD73^{high}, glycolytic areas as GLUT1^{high} (Fig. 3H; Supplementary Fig. S3B and S3C), and hypoxic/glycolytic areas as CD73^{high}GLUT1^{high} (Fig. 3H; Supplementary Fig. S3B and S3C). Most neutrophils (Ly6G^{+}) were found in hypoxic niches (CD73^{high}) compared with nonhypoxic ones (CD73$^{low/neg}$; Fig. 3H and I; Supplementary Fig. S3C–S3E). Although CD71^{-} neutrophils were mostly located in hypoxic/nonglycolytic areas, CD71^{+} neutrophils were largely found in the hypoxic/glycolytic niches of the tumor (Fig. 3H and J; Supplementary Fig. S3C, S3D, S3F).

Altogether, our results suggest that neutrophils are mostly found in the hypoxic regions of brain tumors, and CD71 identifies a glycolytic neutrophil subset that preferentially occupies hypoxic/glycolytic niches.

CD71^{+} Neutrophils Are Mature and Long-Lived Cells with Immunosuppressive Activity in Brain Tumor Beds

Previous studies demonstrated that human BM neutrophil progenitors expressed CD71 (21). To assess the maturation status of neutrophils, we first analyzed the morphology of FACS-sorted tumor-infiltrating Ly6G^{high}CD71^{+} neutrophils by Giemsa staining. We found that most CD71^{+} and CD71^{-} neutrophils from tumors showed a mature-like phenotype (Fig. 3K). In line with these results, CD71^{+} and CD71^{-} neutrophils from tumor tissue and blood were mostly mature cells, based on the expression of CD101 (Supplementary Fig. S3G). However, we observed a higher proportion of CD101^{+} cells in total Ly6G^{high}CD71^{+} and Ly6G^{high}CD71^{-} neutrophils from tumor and blood when compared with BM (Supplementary Fig. S3G). Importantly, we did not find a difference in maturation status between tumor-bearing and naïve mice (Supplementary Fig. S3G), indicating that the presence of the tumor does not affect the maturation status of both subsets of neutrophils. We then analyzed the expression of the chemokine receptors CXCR2 and CXCR4 to further confirm the maturation status of neutrophils (22). CD71^{+} neutrophils displayed higher expression of CXCR2 in brain tumors (Fig. 3L), lower expression in BM, and no differences in blood when compared with CD71^{-} neutrophils (Supplementary Fig. S3H). CD71^{+} neutrophils displayed higher expression of CXCR4 in brain tumors, blood, and BM compared with CD71^{-} neutrophils (Fig. 3L; Supplementary Fig. S3H). Importantly, we did not find any difference between blood and BM of tumor-bearing and naïve mice, respectively (Supplementary Fig. S3H). Thus, CD71^{+} neutrophils are mostly mature neutrophils in blood and in the brain tumor TME.

Next, we sought to investigate the colonization of brain tumors and the lifespan of neutrophil subsets using bromodeoxyuridine (BrdU). Thus, we injected BrdU into mice with brain tumors to first study the dynamics of neutrophil subsets. Colonization of brain tumors by BrdU^{+} neutrophils was observed between days 0 and 4, which represented the peak of BrdU^{+} neutrophil accumulation (Fig. 3M). To assess the survival potential of CD71^{+} neutrophils, we applied a mathematical model of nonlinear regression to calculate the half-life of neutrophils in GBM tissue (23, 24). Of note, the BrdU peak for both subsets was set at 100% (Supplementary Fig. S3I). Thus, CD71^{+} neutrophils exhibited a higher half-life than CD71^{-} neutrophils (5.025 vs. 2.452 days), indicating that these cells have increased survival and persistence within brain tumors (Fig. 3M; Supplementary Fig. S3I).

Next, we assessed the immunosuppressive activity of Ly6G^{high}CD71^{+} neutrophils in brain tumors. To this end, we FACS-sorted these cells from SB28 tumors and tested their ability to suppress the proliferation of anti-CD3–/anti-CD28–activated T cells. Although intratumoral CD71^{+} neutrophils were potent immunosuppressive cells, CD71^{-} neutrophils lacked any suppressive activity (Fig. 3N). Blood-derived CD71^{+} neutrophils also lacked immunosuppressive activity (Supplementary Fig. S4A). Tumor-infiltrating CD71^{+} neutrophils showed higher *Tgfb* and *Vegfa* expression (Supplementary Fig. S4B) as well as PD-L1, CD14, and SIGLECF (Supplementary Fig. S4C), compared with CD71^{-} neutrophils. Of note, CD14 is preferentially expressed by activated polymorphonuclear myeloid-derived suppressor cells (PMN-MDSC; ref. 7). Next, we analyzed the expression of DcTRAIL-R1 (encoded by *Tnfsrf23*), which marks a long-lived neutrophil subset in pancreatic tumors (10). The abundance of DcTRAIL-R1^{+} neutrophils in the blood of naïve mice was similar to that observed in the blood of brain tumor–bearing mice (Supplementary Fig. S4D). However, the abundance of DcTRAIL-R1^{+} neutrophils in brain tumor tissue was higher compared with the periphery (Supplementary Fig. S4D). Most tumor-infiltrating neutrophils were DcTRAIL-R1^{+} (Supplementary Fig. S4D). Importantly, although CD71^{-} and CD71^{+} neutrophils in the blood of naïve and brain tumor–bearing mice expressed similar levels of DcTRAIL-R1 (Supplementary Fig. S4E), only tumor-infiltrating CD71^{+} neutrophils strongly upregulated DcTRAIL-R1 expression compared with tumor-infiltrating CD71^{-} neutrophils (Supplementary Fig. S4E), suggesting that local tumor factors increased the expression of DcTRAIL-R1 specifically in the CD71^{+} neutrophil subset.

Next, we analyzed the distribution of neutrophil subsets in relation to CD3^{+} T cells. A previous study defined a radius of less than 100 μm around T cells as an area with enhanced probabilities of neutrophil–T cell contact. The relative CD3^{+} T-cell density was significantly higher within a distance of 25 μm to suppressive neutrophils compared with "non-suppressive" neutrophils in tumor tissue (25), and T-cell inhibition only happened in close proximity (25). Thus, we quantified neutrophil subsets around CD3^{+} T cells within a radius of 30 μm (Fig. 3O; Supplementary Fig. S4F and S4G). Neutrophils surrounded CD3^{+} T cells, but the frequency of neutrophil subsets was variable among different T cells analyzed (Fig. 3O and P; Supplementary Fig. S4F and S4G), indicating that both subsets may interact with T cells. Thus, these results indicate that the function of a specific subset, rather than its abundance around T cells, may influence T-cell activity in the TME.

Altogether, CD71^{+} neutrophils are mature and long-lived cells that, contrary to CD71^{-} neutrophils, acquire immunosuppressive functions within the brain tumor TME.

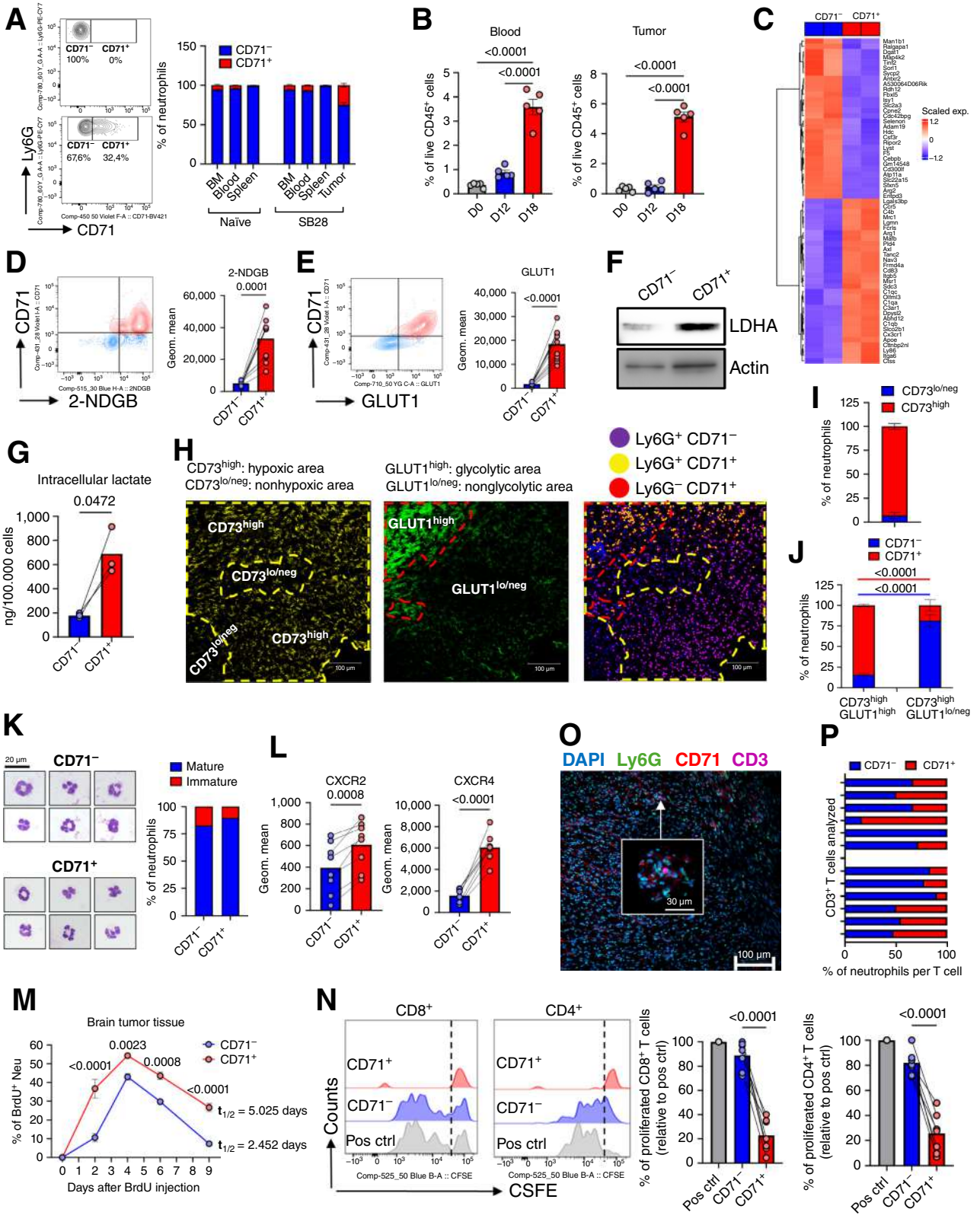

Figure 3. CD71⁺ neutrophils are long-lived, immunosuppressive, and mature cells localized in the hypoxic/glycolytic areas within the brain TME. **A,** Example of murine brain tumor–derived neutrophil gating strategy based on CD71 expression (left) and frequencies of CD71⁺ and CD71⁻ neutrophils in different murine organs (right) by FACS. Naïve $n = 6$, tumor $n = 8$. **B,** Frequency of CD71⁺ neutrophils out of live CD45⁺ cells in blood (left) and tumor (right) of SB28-bearing mice over time by FACS ($n = 5$). **C,** Heatmap of DEGs (30 up and 30 down) in CD71⁻ and CD71⁺ neutrophils (*continued on following page*)

Hypoxia Drives the Immunosuppressive Functions of CD71$^+$ Neutrophils

We then asked whether the brain TME supports the generation of suppressive CD71$^+$ neutrophils from CD71$^-$ neutrophils. To this end, we isolated neutrophils with anti-Ly6G beads from the BM and blood of naïve mice and exposed them to hypoxia (1% O_2) and/or to brain tumor explant supernatant (TES), which was previously used to generate suppressive macrophages (15). After isolation, more than 95% of neutrophils were CD71$^-$ neutrophils (Supplementary Fig. S5A and S5B). Neither TES, hypoxia, nor the combination induced CD71 expression in neutrophils (Supplementary Fig. S5A and S5B). CD71$^-$ neutrophils, FACS-sorted from mouse brain tumors, also failed to express CD71 upon stimulation with hypoxia and/or TES, alone or in combination (Supplementary Fig. S5C). Similarly, hypoxia did not induce CD71 expression in neutrophils from the blood of human patients with GBM (Supplementary Fig. S5D). Importantly, CD71$^-$ neutrophils did not acquire suppressive activity upon stimulation with either hypoxia and/or TES (Supplementary Fig. S5E). To further prove that CD71$^-$ neutrophils did not differentiate into CD71$^+$ neutrophils within the TME, we adoptively transferred CD71$^-$ neutrophils (CD45.1), isolated from naïve BM, into tumors (SB28) established subcutaneously in recipient CD45.2 mice. By FACS, we found that CD71$^-$ neutrophils did not differentiate into CD71$^+$ neutrophils in the TME (Supplementary Fig. S5F). Thus, hypoxia and tumor-derived factors did not support CD71 expression and the suppressive activity in neutrophils, suggesting that CD71$^-$ neutrophils might not be converted into immunosuppressive CD71$^+$ neutrophils.

As CD71$^+$ neutrophils did not differentiate from CD71$^-$ neutrophils, we asked whether CD71$^+$ neutrophils could be generated from BM precursors. Using the setting shown in Supplementary Fig. S5G, we found a significant proportion of CD71$^+$ neutrophils after 6 days of BM cell culture with GM-CSF. CD71$^+$ neutrophils were produced by the BM, regardless of the presence of either hypoxia or tumor-derived factors, confirming that neither hypoxia nor TES supported the expansion of these cells (Fig. 4A). In addition, most neutrophils generated in normoxic conditions demonstrated a mature-like phenotype; however, hypoxia induced further maturation of both CD71$^-$ and CD71$^+$ neutrophils (Supplementary Fig. S5H and S5I). To further show that CD71$^+$ neutrophils are generated from BM precursors, we analyzed CD71$^+$ neutrophil appearance from neutrophil progenitors [pro-neutrophils (proNeu)], which were FACS-sorted from the BM of naïve mice, as previously shown (Fig. 4B; ref. 26), and cultured with GM-CSF for 6 days. ProNeu were all Ly6G$^-$CD71$^+$, indicating that distinct progenitors might not be identified based on CD71 expression (Fig. 4C). CD11B^{high}Ly6G$^+$ neutrophils started differentiating from proNeu on day 2 and represented most of the cells in culture on day 6 (more than 80%). Both CD71$^-$ and CD71$^+$ neutrophils appeared on day 2 as well and continued accumulating over time (Fig. 4D and E). Thus, CD71$^+$Ly6G$^+$ neutrophils appeared at early time points during neutrophil differentiation from proNeu.

Next, we sought to assess whether *in vitro*–generated CD71$^+$ neutrophils exposed to hypoxia mirror *in vivo* CD71$^+$ neutrophils from brain tumors. To this end, we first performed bulk RNA-seq of *in vitro* hypoxic neutrophils. We found 1,440 DEGs, of which 787 were upregulated ($\log_2$FC > 1 and adjusted $P < 0.05$) and 653 were downregulated ($\log_2$FC < −1 and adjusted $P < 0.05$) in CD71$^+$ neutrophils compared with CD71$^-$ neutrophils (Fig. 4F). Then, seeking to determine to what extent the gene expression of CD71$^+$ neutrophils isolated from brain tumors was recapitulated in *in vitro* hypoxic CD71$^+$ neutrophils, we first found a significant overlap of 606 genes (2-fold more than random) among DEGs (CD71$^+$ vs. CD71$^-$ neutrophils) between *in vivo* and *in vitro* neutrophils (Fig. 4G). Then, by using Spearman correlation coefficients, we found high similarity between *in vitro* CD71$^+$ neutrophils and *in vivo* (brain tumor) CD71$^+$ neutrophils, as well as between *in vitro* CD71$^-$ neutrophils and *in vivo* CD71$^-$ neutrophils (Fig. 4H). Thus, our data suggest that *in vivo* CD71$^+$ neutrophils are mirrored *in vitro* by exposure to hypoxia.

Next, we asked whether hypoxia or TES supported CD71$^+$ neutrophil immunosuppressive activity. Using the model shown in Supplementary Fig. S5G, we exposed *in vitro*–generated neutrophils to hypoxia or TES during the last 3 days of culture. Then, FACS-sorted CD71$^-$ and CD71$^+$

Figure 3. ***(Continued)*** (FACS-sorted from SB28 brain tumors) by bulk RNA-seq. Shown are Z-scale gene expression levels. **D,** 2-2-(N-(7-nitrobenz-2-oxa-1,3-diazol-4-yl)amino)-2-deoxyglucose (NDGB) uptake in murine tumor (SB28)–derived neutrophils measured by FACS and expressed as Geometric (geom) mean FC to CD71$^-$ neutrophils ($n = 10$). **E,** GLUT1 expression in murine tumor (SB28)–derived neutrophils measured by FACS and expressed as geom. mean FC to CD71$^-$ neutrophils ($n = 12$). **F,** WB of indicated markers in tumor (SB28)–derived neutrophils ($n = 10$). **G,** Intracellular lactate levels in *in vivo* neutrophils (lactate assay kit). Each replicate ($n = 3$) represents cumulative results of neutrophils from 2 to 3 mice pooled together, for a total of $n = 8$ mice. **H,** Localization of neutrophils in specific areas of brain tumors. Scale bar, 100 μm. CD73 single staining is shown to identify hypoxic areas (left). GLUT1 single staining is shown to identify glycolytic areas (middle). CD71$^-$ neutrophil (Ly6G$^+$CD71$^-$, purple), CD71$^+$ neutrophil (Ly6G$^+$CD71$^+$, yellow), and CD71$^+$ non-neutrophil cells (Ly6G$^-$CD71$^+$, red) were identified using the Nikon NIS-Elements Advanced Research (version 6.02.01) Build 1973 and the Bright Spot Detection tool (nuclei are shown in blue; right). **I,** Frequency of neutrophils (Ly6G$^+$ cells) in indicated areas of GBM tumors. Cells were counted with the auto measurement tool using the Nikon NIS-Elements Advanced Research (version 6.02.01) Build 1973 and the Bright Spot Detection tool ($n = 4$). **J,** Frequency of neutrophil subsets in indicated areas of GBM tumors. Cells were counted with the auto measurement tool using the Nikon NIS-Elements Advanced Research (version 6.02.01) Build 1973 and the Bright Spot Detection tool ($n = 4$). **K,** Giemsa staining (left) and proportion of mature/immature cells (right) in tumor (SB28)–derived neutrophils. **L,** CXCR2 (left) and CXCR4 (right) expression by tumor (SB28)–derived neutrophils by FACS ($n = 8$). **M,** Analysis of BrdU$^+$ neutrophil subsets in SB28 brain tumors over time after a single injection of BrdU (D0). Shown is the calculated half-life ($t_{1/2}$) of each subset after reaching the BrdU peak at D4. $n = 5$ mice per time point. **N,** Suppressive ability of mouse tumor (SB28)–derived CD71$^+$ and CD71$^-$ neutrophils on CD8$^+$ and CD4$^+$ T-cell proliferation, measured as CFSE dilution by FACS. Each replicate ($n = 7$) represents cumulative results of neutrophils from 2 to 3 mice pooled together, for a total of $n = 18$ mice. **O,** Localization of neutrophils around CD3$^+$ T cells within a radius of 30 μm. A merged image of DAPI, Ly6G, CD71, and CD3 staining is shown. **P,** Frequencies of neutrophil subsets out of total neutrophils per single CD3$^+$ T cell. Thirteen CD3$^+$ T cells were identified in six different sections from two different tumors, and neutrophils were counted in the surrounding area within a radius of 30 μm. All data are presented as mean ± SEM. Statistical analysis was performed using one-way ANOVA with Tukey's *post hoc* test (**B**), paired two-sided Student *t* tests (**D**, **E**, **G**, **L**, and **N**), and the mathematical model of nonlinear regression to calculate cells' K constant and half-life with the associated *P* value (**M**).

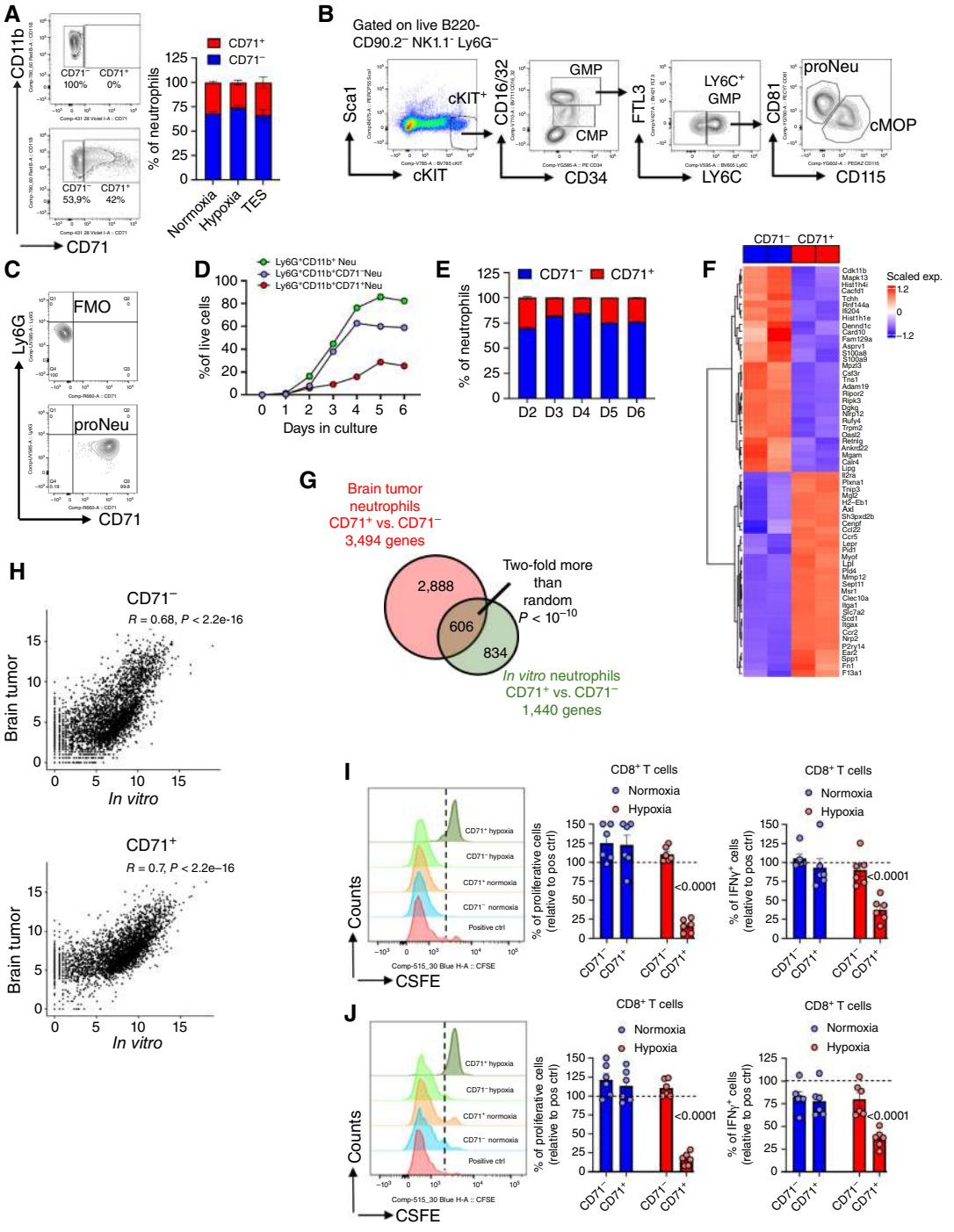

Figure 4. Hypoxia drives the immunosuppressive functions of CD71⁺ neutrophils. **A,** Example of *in vitro* neutrophil gating strategy based on CD71 expression (left) and frequencies of CD71⁺ and CD71⁻ neutrophils *in vitro* (right) by FACS. $n = 14$ (TES, $n = 4$). **B,** Gating strategy used to identify and sort neutrophil progenitors (proNeu). **C,** Ly6G and CD71 expression by proNeu before *in vitro* culture with GM-CSF, by FACS. FMO = Fluorescence Minus One control. **D,** Analysis of the frequencies of total neutrophils and neutrophil subsets out of live cells over time during the *in vitro* differentiation with GM-CSF, by FACS ($n = 2$). **E,** Analysis of the frequencies of neutrophil subsets out of total neutrophils during the *in vitro* differentiation with GM-CSF, by FACS ($n = 2$). **F,** Heatmap of DEGs (30 up and 30 down) in CD71⁻ and CD71⁺ neutrophils (FACS sorted from *in vitro* cultures under hypoxic conditions) by bulk RNA-seq. Shown are Z-scale gene expression levels. **G,** Overlap of significantly DEGs between neutrophils FACS-sorted from the *in vitro* model under hypoxic conditions and from brain tumors. **H,** Similarity between *in vitro* CD71⁺ and *in vivo* CD71⁺ neutrophils, as well as between CD71⁻ *in vitro* and CD71⁻ *in vivo* neutrophils. **I,** Suppressive ability of *in vitro* CD71⁺ and CD71⁻ neutrophils on CD8⁺ T-cell proliferation (left, measured as CFSE dilution) and IFNγ production (right), by FACS ($n = 6$). **J,** Suppressive ability of *in vitro* CD71⁺ and CD71⁻ neutrophils on CD4⁺ T-cell proliferation (left, measured as CFSE dilution) and IFNγ production (right), by FACS ($n = 6$). All data are presented as mean ± SEM. Statistical analysis was performed using Spearman correlation coefficients with the associated *P* value (**H**) and two-way ANOVA with Tukey's *post hoc* test (**I** and **J**). In **G,** a permutation test was performed to calculate an empirical *P* value.

neutrophils were assayed for their ability to suppress T-cell proliferation and IFNγ production. TES-treated CD71$^+$ neutrophils did not acquire the ability to suppress either proliferation or IFNγ production of T cells (Supplementary Fig. S5J). However, hypoxia-treated CD71$^+$ neutrophils acquired a potent ability to suppress the proliferation and IFNγ production by both CD4$^+$ and CD8$^+$ T cells, compared with CD71$^+$ neutrophils from normoxic conditions and with hypoxic CD71$^-$ neutrophils (Fig. 4I and J). Of note, hypoxic CD71$^-$ and CD71$^+$ neutrophils showed similar levels of HIF1α (Supplementary Fig. S5K). Our data indicate that hypoxia, but not soluble tumor-derived factors, promoted the immunosuppressive activity of CD71$^+$ neutrophils. Moreover, similarly to CD71$^+$ neutrophils from brain tumors, hypoxic CD71$^+$ neutrophils demonstrated higher *Vegf*a and *Tgf*b levels by qRT-PCR (Supplementary Fig. S5L) compared with hypoxic CD71$^-$ neutrophils and with normoxic CD71$^-$ and CD71$^+$ neutrophils. However, no differences in inducible nitric oxide synthetase expression (Supplementary Fig. S5M) and in the hypoxic CD71$^-$ and CD71$^+$ neutrophil viability were observed (Supplementary Fig. S6A). Both subsets died over time during the coculture with CD3$^+$ T cells. However, hypoxic CD71$^+$ neutrophils seem more resistant to cell death compared with hypoxic CD71$^-$ neutrophils (Supplementary Fig. S6B) under such conditions.

As tumor CD71$^+$ neutrophils showed prolonged survival in the TME, we determined whether hypoxia sustained CD71$^+$ neutrophils. To this end, we adoptively transferred hypoxic and normoxic neutrophil subsets (CD45.2) into naïve congenic mice (CD45.1; Supplementary Fig. S6C). After 24 hours, we quantified adoptively transferred neutrophils in blood, spleen, and lung tissues using counting beads by FACS. Normoxic subsets were mostly absent in all organs/tissues analyzed. Hypoxic CD71$^-$ and CD71$^+$ neutrophils were largely found in lung tissue compared with other organs and tissues. However, the number of hypoxic CD71$^+$ neutrophils was significantly higher in lung tissue compared with hypoxic CD71$^-$ neutrophils (Supplementary Fig. S6D). Thus, hypoxia may sustain both subsets within tissues. The fact that hypoxic CD71$^+$ neutrophils were found in higher numbers in lungs compared with hypoxic CD71$^-$neutrophils further indicates that hypoxia may preferentially sustain to immunosuppressive CD71$^+$ neutrophils within the tissue.

ARG1 Supports CD71$^+$ Neutrophil Immunosuppressive Activity

We then asked how hypoxic CD71$^+$ neutrophils suppress T-cell activity. In our bulk RNA-seq, among the most upregulated genes, *Arg1* was highly expressed by brain tumor–infiltrating CD71$^+$ neutrophils (Fig. 3C). As arginase-1 (ARG1) is a major contributor to the immunosuppressive activity of neutrophils (7, 18, 27, 28), we analyzed ARG1 expression in CD71$^+$ neutrophils. Hypoxic CD71$^+$ neutrophils *in vitro* demonstrated high expression of ARG1 by qRT-PCR (Fig. 5A) and western blot (WB) (Fig. 5B), compared with hypoxic CD71$^-$ neutrophils and with normoxic CD71$^-$ and CD71$^+$ neutrophils. Then, we asked whether hypoxic CD71$^+$ neutrophils used ARG1 to suppress T-cell activity. To this end, we inhibited ARG1 with the arginine analogue Nω-hydroxy-nor-L-arginine (norNOHA) during the coculture of neutrophils and T cells. We found that treatment with norNOHA affected the ability of hypoxic CD71$^+$ neutrophils to suppress the proliferation and IFNγ production of T cells (Fig. 5C and D), indicating the key role of ARG1 in mediating the suppressive ability of hypoxic CD71$^+$ neutrophils.

To assess the relevance of ARG1 *in vivo*, we analyzed the expression of ARG1 in brain tumor CD71$^+$ neutrophils. Like hypoxic CD71$^+$ neutrophils *in vitro*, brain tumor CD71$^+$ neutrophils demonstrated high expression of ARG1 by qRT-PCR and WB (Fig. 5E and F). Next, to test the hypothesis that CD71$^+$ neutrophils from the circulation acquire ARG1 expression once they reach the tumor, we adoptively transferred FACS-sorted CD71$^-$ and CD71$^+$ neutrophils from the BM of naïve CD45.1 mice into SB28 tumors established subcutaneously in CD45.2 mice. After 3 days, we FACS-sorted the adoptively transferred CD45.1 CD71$^-$ and CD71$^+$ neutrophils from tumors, and we analyzed the expression of *Arg1* (Fig. 5G). By qRT-PCR, we found that CD71$^+$ neutrophils critically upregulated the expression of *Arg1* compared with CD71$^-$ neutrophils upon adoptive transfer into the tumor (Fig. 5G). Thus, our results suggest that circulating neutrophils acquire features of immunosuppressive cells within the TME. To demonstrate that brain tumor CD71$^+$ neutrophils suppressed T cells in an ARG1-dependent manner, we analyzed the suppressive ability of CD71$^+$ neutrophils, FACS-sorted from brain tumors of mice treated with norNOHA. norNOHA affected the ability of CD71$^+$ neutrophils to suppress T-cell proliferation, suggesting that ARG1 plays a key role in the function of CD71$^+$ neutrophils in brain tumors (Fig. 5H).

Next, we sought to verify the role of CD71 in the regulation of the immunosuppressive activity of neutrophils in GBM tumors. To this end, we created neutrophil-specific conditional knockout (CKO) mice deficient in CD71 (encoded by the *Tfrc* gene) by crossing *Tfrc*$^{fl/fl}$ with *S100A8-**Cre**$^+$* mice (*Tfrc*$^{fl/fl}$ Cre$^+$), which resulted in a total loss of CD71 in neutrophils *in vivo* (Supplementary Fig. S6E). FACS-sorted neutrophils from brain tumors established in control (*Tfrc*$^{fl/fl}$ Cre$^-$) and CD71 CKO (*Tfrc*$^{fl/fl}$ Cre$^+$) mice were assayed for their ability to suppress the proliferation of T cells. We found that *Tfrc*$^{fl/fl}$ Cre$^+$ neutrophils suppressed the proliferation of CD4$^+$ and CD8$^+$ T cells to the same extent as control *Tfrc*$^{fl/fl}$ Cre$^-$ neutrophils (Supplementary Fig. S6F), suggesting that CD71 does not regulate the suppressive functions of neutrophils in GBM tumors. Additionally, the absence of CD71 in neutrophils did not improve the survival of mice with brain tumors (Supplementary Fig. S6G). In parallel, we also analyzed the role of CD71 *in vitro*. Thus, neutrophils differentiated from the BM of *Tfrc*$^{fl/fl}$ Cre$^+$ mice and treated with hypoxia were tested in T-cell suppression assays. *Tfrc*$^{fl/fl}$ Cre$^+$ neutrophils lost the expression of CD71 (Supplementary Fig. S6H), but they preserved the ability to suppress the proliferation and IFNγ production by T cells (Supplementary Fig. S6I). Importantly, no changes in ARG1 were observed in *Tfrc*$^{fl/fl}$ Cre$^+$ neutrophils (Supplementary Fig. S6H). Our data indicate that CD71 is not required for the acquisition of suppressive functions by CD71$^+$ neutrophils. Taken together, our results suggest that hypoxia is a major driver of the suppressive ability of CD71$^+$ neutrophils in GBM tumors.

Glucose and Lactate Drive the Immunosuppressive Activity of CD71+ Neutrophils

The N3 cluster demonstrated higher enrichment in glycolysis and hypoxia compared with N1 and N2 from tumors and blood, respectively (Fig. 5I). As brain tumor–infiltrating GLUT1-deficient macrophages and neutrophils showed impaired immunosuppressive ability (15), we hypothesized that hypoxia may drive the metabolic reprogramming of CD71+ neutrophils in the TME, ultimately leading to an immunosuppressive phenotype. Toward this goal, neutrophils from *in vitro* cultures were assayed for their metabolic profile by the Seahorse extracellular flux analyzer. By a Seahorse Mito Stress Test, we did not observe significant differences in the basal oxygen consumption rate (OCR), as an indicator of mitochondrial respiration, between CD71− and CD71+ neutrophils from normoxic and hypoxic conditions (Supplementary Fig. S7A and S7B). CD71+ neutrophils, regardless of hypoxia, showed higher spare respiratory capacity, a key indicator of mitochondrial function, compared with CD71− neutrophils (Supplementary Fig. S7B). However, normoxic CD71+ neutrophils showed a higher basal extracellular acidification rate, as an indicator of glycolysis, which was boosted by hypoxia, compared with normoxic CD71− neutrophils (Supplementary Fig. S7C). By a Seahorse Glycolysis Stress Test, we confirmed that hypoxic CD71+ neutrophils showed higher glycolysis and glycolytic capacity than hypoxic CD71− neutrophils, as well as normoxic CD71− and CD71+ neutrophils (Fig. 5J). The enhanced glycolytic profile of hypoxic CD71+ neutrophils correlated with higher GLUT1 and LDHA expression, compared with hypoxic CD71−neutrophils and normoxic CD71− and CD71+ neutrophils (Fig. 5K). This, in turn, resulted in a higher intracellular lactate accumulation in hypoxic CD71+ neutrophils (Fig. 5L), similar to what we found *in vivo* in CD71+ neutrophils. Thus, CD71+ neutrophils are innately more glycolytic than CD71− neutrophils, and this glycolytic profile is boosted by hypoxia.

To verify if CD71 regulated glucose metabolism in neutrophils, we analyzed glycolysis and glycolytic capacity in control and CD71 CKO neutrophils using the Seahorse Glycolysis Stress Test. We found that CD71 CKO neutrophils showed higher glycolysis and glycolytic capacity compared with control neutrophils (Supplementary Fig. S7D). Thus, CD71 is not required for the acquisition of the glycolytic phenotype observed in hypoxic CD71+ neutrophils.

Next, we assessed GLUT1's contribution to the immunosuppressive ability of CD71+ neutrophils from brain tumors established in *Slc2a1*$^{fl/fl}$ *Lyz2-Cre*+ mice (GLUT1 CKO). By FACS, we found no differences in the frequency of CD71+ neutrophils in tumors established in either control or GLUT1 CKO mice (Supplementary Fig. S7E), as well as in CD71 expression (Supplementary Fig. S7F). Then, we found that FACS-sorted GLUT1 CKO CD71+ neutrophils lost their ability to suppress CD4+ and CD8+ T-cell proliferation compared with their counterparts from control mice, highlighting a role for glucose in the regulation of CD71+ neutrophil immunosuppressive function (Fig. 5M).

To determine the contribution of glucose metabolism to the suppressive activity of CD71+ neutrophils, we analyzed the immunosuppressive activity of *in vitro*–generated hypoxic CD71+ neutrophils following treatment with 2-deoxy-D-glucose (2-DG), a glycolysis inhibitor. The inhibition of glycolysis resulted in the impaired ability of CD71+ neutrophils to suppress the proliferation and IFNγ production by both CD8+ (Fig. 5N) and CD4+ (Supplementary Fig. S8A) T cells.

As CD71+ neutrophils also showed high LDHA expression and enhanced intracellular lactate accumulation, we inhibited the production of lactate using GNE-140, a specific inhibitor of LDHA, to assess the contribution of intracellular lactate to the immunosuppressive activity of CD71+ neutrophils. The inhibition of LDHA resulted in the inability of hypoxic CD71+ neutrophils to suppress the proliferation and IFNγ production by both CD8+ (Fig. 5O) and CD4+ (Supplementary Fig. S8B) T cells. Importantly, the inhibition of either glycolysis or lactate production resulted in the inhibition of ARG1 expression at both mRNA (Fig. 5P) and protein levels (Fig. 5Q).

Taken together, our results suggest that glucose and lactate production are drivers of the immunosuppressive activity of hypoxic CD71+ neutrophils.

Figure 5. Hypoxia-driven glucose metabolism and intracellular lactate production govern the immunosuppressive functions of CD71+ neutrophils through ARG1. **A,** *Arg1* expression by qRT-PCR in *in vitro* neutrophils. Normoxia $n = 4$, hypoxia $n = 7$. **B,** WB of indicated markers in *in vitro* neutrophils. **C,** Suppressive ability of *in vitro* hypoxic CD71+ and CD71− neutrophils treated with norNOHA on CD8+ T-cell proliferation (left, measured as CFSE dilution) and IFNγ production (right), by FACS ($n = 3$). **D,** Suppressive ability of *in vitro* hypoxic CD71+ and CD71− neutrophils treated with norNOHA on CD4+ T-cell proliferation (left, measured as CFSE dilution) and IFNγ production (right) by FACS ($n = 3$). **E,** *Arg1* expression by tumor (SB28)–derived neutrophils by qRT-PCR. Each replicate ($n = 14$) represents cumulative results of neutrophils from 2 to 3 mice pooled together, for a total of $n = 35$ mice. **F,** WB of indicated markers in tumor (SB28)–derived neutrophils ($n = 10$). **G,** Gating strategy used to identify and sort by FACS CD45.1 CD71+ and CD71− neutrophils adoptively transferred intratumorally into SB28 (s.c.) tumor-bearing CD45.2 mice and *Arg1* expression by qRT-PCR in CD71+ and CD71− neutrophils before (D0) and after (D3) the intratumor adoptive transfer. FMO = Fluorescence Minus One control. **H,** Suppressive ability of CD71+ neutrophils FACS-sorted from vehicle- versus norNOHA-treated mice on CD4+ (left) and CD8+ (right) T-cell proliferation, measured as CFSE dilution by FACS ($n = 3$). **I,** Violin plots comparing glucose metabolism and hypoxia gene set expression between blood versus tumor samples in different neutrophil clusters. **J,** Representative glycolysis stress test kinetic plot, wherein values for extracellular acidification rate (ECAR, mpH/minute) are plotted versus time (left; note that glucose was injected at 18 minutes, followed by oligomycin A injection at 36 minutes and 2-DG injection at 54 minutes); summaries of ECAR data representative of the glycolytic capacity (middle) and glycolysis (right). $n = 3$. **K,** WB of indicated markers in *in vitro* neutrophils. **L,** Intracellular lactate levels in *in vitro* neutrophils (lactate assay kit). $n = 4$. **M,** Suppressive ability of CD71+ and CD71− neutrophils FACS-sorted from control (*Slc2a1*$^{fl/fl}$ *Lyz2-Cre*−) versus GLUT1 CKO (*Slc2a1*$^{fl/fl}$ *Lyz2-Cre*+) mice on CD8+ (left) and CD4+ (right) T-cell proliferation, measured as CFSE dilution by FACS ($n = 3$). **N,** Suppressive ability of *in vitro* CD71+ and CD71− neutrophils treated with 2-DG on CD8+ T-cell proliferation (left; measured as CFSE dilution) and IFNγ production (right), by FACS ($n = 3$). **O,** Suppressive ability of *in vitro* CD71+ and CD71− neutrophils treated with GNE-140 on CD8+ T-cell proliferation (left; measured as CFSE dilution) and IFNγ production (right), by FACS ($n = 3$). **P,** *Arg1* expression by qRT-PCR in *in vitro* hypoxic CD71+ and CD71− neutrophils treated with 2-DG (left, $n = 3$) and GNE-140 (right, $n = 4$). **Q,** WB of indicated markers in *in vitro* hypoxic neutrophils treated with 2-DG and GNE-140. All data are presented as mean ± SEM. Statistical analysis was performed using two-way ANOVA with Tukey's *post hoc* test (**A**, **C**, **D**, **G**, **H**, **J**, **L**, **M**, **N**, **O**, and **P**), paired two-sided Student *t* tests (**E**), and one-way ANOVA with Tukey's *post hoc* test (**H**).

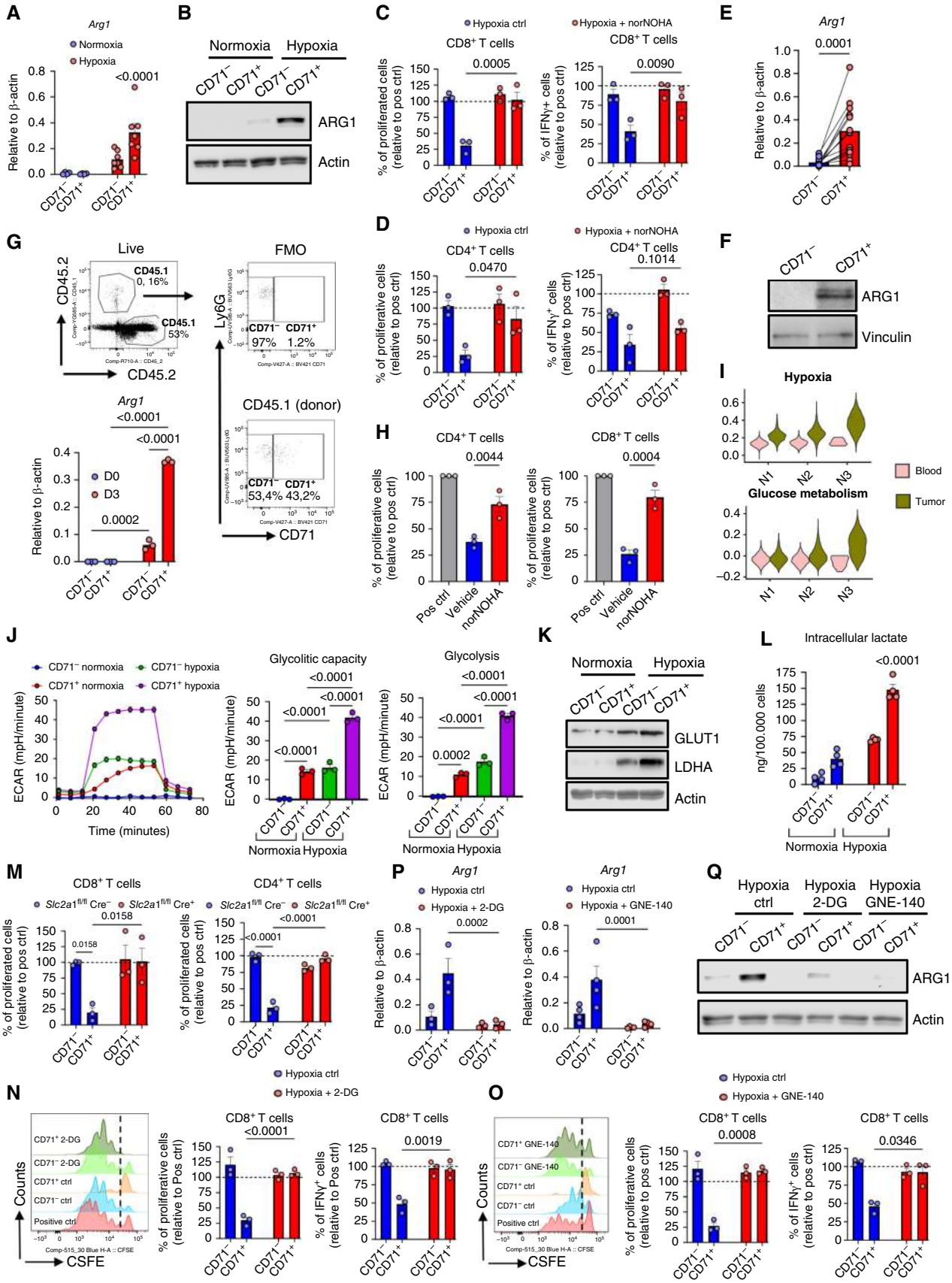

Histone Lactylation Regulates ARG1 Expression in Immunosuppressive CD71+ Neutrophils

Next, we asked how glucose and lactate govern ARG1-mediated immunosuppressive activity in hypoxic CD71+ neutrophils. A recent study demonstrated that glucose is incompletely oxidized to produce lactate, which generates lactyl-CoA. This lactyl-CoA acts to add a lactyl group to the lysine tails of histone proteins via the acetyltransferase enzyme p300 to produce a modification called histone lactylation (Kla; ref. 29). Kla promoted gene expression in M1-like macrophages (29), macrophages after myocardial infarction (30), and immunosuppressive MDM in GBM tumors (15). Thus, we analyzed Kla in glycolytic CD71+ neutrophils isolated from mouse brain tumors. We found that glycolytic CD71+ neutrophils showed higher Kla levels compared with CD71− neutrophils, with no differences in histone acetylation (Kac) levels (Fig. 6A). Using a CUT&RUN assay with an anti–pan-Kla antibody followed by qRT-PCR, we found high levels of Kla marks at the promoter of the *Arg1* gene (Fig. 6B). In addition, we analyzed Kla levels in hypoxic CD71+ neutrophils *in vitro*. We found that hypoxic CD71+ neutrophils demonstrated higher Kla levels compared with hypoxic CD71− neutrophils and normoxic CD71− and CD71+ neutrophils (Fig. 6C), whereas the levels of lysine acetylation (Kac) were similar between all the conditions (Fig. 6C).

Next, we asked whether glycolysis and lactate sustained Kla in hypoxic CD71+ neutrophils. Upon treatment with either 2-DG or GNE-140, hypoxic CD71+ neutrophils demonstrated a drastic reduction of Kla levels by WB (Fig. 6D), compared with controls. Using a CUT&RUN assay with an anti–Pan Kla antibody followed by qRT-PCR, we found high levels of Kla marks at the promoter of the *Arg1* gene in hypoxic CD71+ neutrophils compared with hypoxic CD71− neutrophils (Fig. 6E). Importantly, the inhibition of either glycolysis or lactate production significantly reduced Kla marks at the promoter of *Arg1* (Fig. 6E). In parallel, to assess the contribution of extracellular lactate to Kla, we first analyzed the expression of monocarboxylate transporter 1 (MCT1) and MCT2, which are major transporters for lactate influx (31, 32). Neutrophils also express MCT4, which is mostly involved in lactate efflux (33). Although we did not observe a difference in MCT2 expression, normoxic and hypoxic CD71+ neutrophils demonstrated high expression of MCT1 compared with CD71− neutrophils (Supplementary Fig. S8C). However, normoxic and hypoxic CD71+ neutrophils expressed similar levels of MCT2 (Supplementary Fig. S8C). Next, we analyzed the suppressive activity of hypoxic CD71+ neutrophils upon inhibition of extracellular lactate uptake using AZD3965 (30), a potent and selective MCT1 inhibitor. Of note, AZD3965 also exhibits some inhibitory activity against MCT2 (34, 35). Upon treatment with the MCT1 inhibitor, we did not observe changes in Kla (Supplementary Fig. S8D), ARG1 expression (Supplementary Fig. S8D), and suppressive activity (Supplementary Fig. S8E) of hypoxic CD71+ neutrophils, indicating that extracellular lactate uptake does not support Kla and the immunosuppressive function of hypoxic CD71+ neutrophils.

Next, to determine whether glucose is a source for Kla, we analyzed the incorporation of ^{13}C into lactylated histones in *in vitro* normoxic and hypoxic neutrophils cultured with U-$^{13}C_6$-glucose, using mass spectrometry (MS). The levels of ^{13}C-labeled lactylated histone 3 were higher in hypoxic CD71+ neutrophils compared with hypoxic CD71− neutrophils and with normoxic CD71− and CD71+ neutrophils (Fig. 6F), indicating that glucose is a source for Kla in hypoxic CD71+ neutrophils.

The acetyltransferase enzyme p300 is a potential Kla writer protein; therefore, we investigated the impact of p300 inhibition on Kla and on the function of hypoxic CD71+ neutrophils. CPI-1612, a potent and selective inhibitor of p300, reduced Kla levels in hypoxic CD71+ neutrophils (Fig. 6G) and reduced Kla marks at the promoter of *Arg1* by CUT&RUN assay (Fig. 6H), which was accompanied by impaired expression of ARG1 at both the mRNA and protein levels (Fig. 6G and I) and by the inability of hypoxic CD71+ neutrophils to suppress the proliferation and IFNγ production of both CD8+ and CD4+ T cells (Fig. 6J; Supplementary Fig. S8F). No differences were observed in Kac levels at the promoter of *Arg1* (Supplementary Fig. S8G). Our data suggest that Kla plays a role in the acquisition of immunosuppressive function by hypoxic CD71+ neutrophils.

To verify the potential contribution of Kac to the immunosuppressive activity of CD71+ neutrophils, we treated hypoxic neutrophils with BMS-303141, an inhibitor of ATP citrate lyase (ACLY) that generates acetyl–CoA as a substrate for nuclear Kac (36, 37). Although BMS-303141 treatment affected Kac levels, CD71+ neutrophils did not show defective immunosuppressive ability or ARG1 expression (Supplementary Fig. S8H–S8J).

Taken together, hypoxia-driven glucose metabolism promotes the immunosuppressive ability of CD71+ neutrophils via Kla, which regulates ARG1 expression in these cells.

Isosafrole Impairs the Kla-Driven Immunosuppressive Ability of CD71+ Neutrophils and Boosts the Efficacy of Immunotherapy

We sought to determine whether targeting LDHA could reduce lactate production and Kla levels in tumor-infiltrating CD71+ neutrophils, resulting in the inability of these cells to suppress antitumor immunity and a consequent improvement in the survival of mice with brain tumors. To this end, we employed isosafrole, an analog of the antiepileptic drug stiripentol with high blood-brain barrier penetrance, which was used to suppress lactate-dependent seizures in a murine model (38, 39). First, we treated hypoxic neutrophils generated *in vitro* with isosafrole and found that the treatment with isosafrole inhibited LDHA in hypoxic CD71+ neutrophils, thus resulting in reduced Kla and ARG1 levels (Fig. 6K; Supplementary Fig. S9A) and in the consequent inability of hypoxic CD71+ neutrophils to suppress the proliferation and IFNγ production of both CD8+ and CD4+ T cells (Fig. 6L; Supplementary Fig. S9B). However, treatment with isosafrole did not affect the suppressive function of *in vitro*–generated immunosuppressive macrophages (Supplementary Fig. S9C), the proliferation of CD8+ and CD4+ T cells (Supplementary Fig. S9D), or tumor cell proliferation and survival (Supplementary Fig. S9E). Importantly, isosafrole did not affect the viability of neutrophil subsets (Supplementary Fig. S9F). Thus, isosafrole preferentially targets hypoxic CD71+ neutrophils.

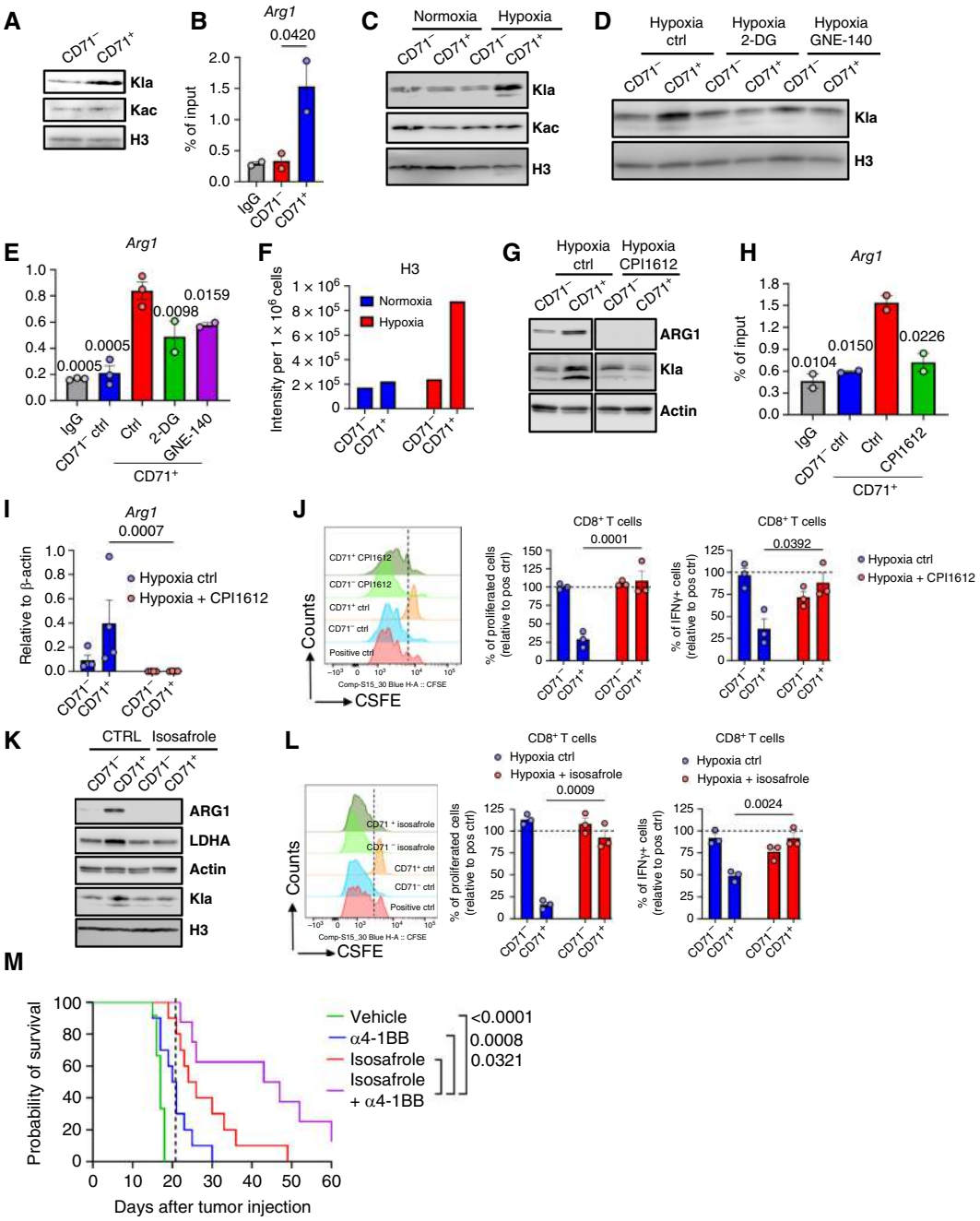

Figure 6. Histone lactylation governs ARG1 expression in CD71⁺ neutrophils. **A,** WB of indicated markers in tumor (SB28)-derived neutrophils ($n = 10$). **B,** CUT&RUN-qRT-PCR analysis for the association of Kla with the promoter of the *Arg1* gene in tumor-derived neutrophils. Each replicate ($n = 2$) represents cumulative results of neutrophils from five mice pooled together, for a total of $n = 10$ mice. **C,** WB of indicated markers in *in vitro* neutrophils. **D,** WB of indicated markers in *in vitro* hypoxic neutrophils treated with 2-DG and GNE-140. **E,** CUT&RUN-qRT-PCR analysis for the association of Kla with the promoter of the *Arg1* gene in *in vitro* hypoxic neutrophils treated with 2-DG and GNE-140. Each replicate (control $n = 3$, 2-DG and GNE-140 $n = 2$) represents cumulative results of neutrophils from two mice pooled together, for a total of $n = 6$ mice (control) and $n = 4$ mice (2-DG and GNE-140). **F,** ^{13}C incorporation in lysine-lactylated histone 3 in *in vitro* neutrophils loaded with U-$^{13}C_6$-glucose. Neutrophils from four different mice were pooled together, and lysine-lactylated histones were isolated. Cumulative results of total heavy Kla histone 3 (H3; normalized per million cells) are shown ($n = 4$). **G,** WB of indicated markers in *in vitro* hypoxic neutrophils treated with CPI1612. **H,** *Arg1* expression by qRT-PCR in *in vitro* hypoxic CD71⁺ and CD71⁻ neutrophils treated with CPI1612 ($n = 4$). **I,** Suppressive ability of *in vitro* CD71⁺ and CD71⁻ neutrophils treated with CPI1612 on CD8⁺ T-cell proliferation (left; measured as CFSE dilution) and IFNγ production (right), by FACS ($n = 3$). **J,** CUT&RUN-qRT-PCR analysis for the association of Kla with the promoter of the *Arg1* gene in *in vitro* hypoxic neutrophils treated with CPI1612. Each replicate ($n = 2$) represents cumulative results of neutrophils from two mice pooled together, for a total of $n = 4$ mice. **K,** WB of indicated markers in *in vitro* hypoxic neutrophils after treatment with isosafrole. **L,** Suppressive ability of *in vitro* CD71⁺ and CD71⁻ neutrophils treated with isosafrole on CD8⁺ T-cell proliferation (left; measured as CFSE dilution) and IFNγ production (right), by FACS ($n = 3$). **C,** Kaplan–Meier representation of SB28-bearing mice survival treated with vehicle ($n = 12$), α4-1BB ($n = 10$), and isosafrole ($n = 10$) alone or in combination ($n = 8$). The dashed line indicates the end of treatment. All data are presented as mean ± SEM. Statistical analysis was performed using two-way ANOVA with Holm–Šidák's *post hoc* test (**B**, **E**, and **J**), two-way ANOVA with Tukey's *post hoc* test (**H**, **I**, and **L**), and the Kaplan–Meier method and log-rank test (**M**).

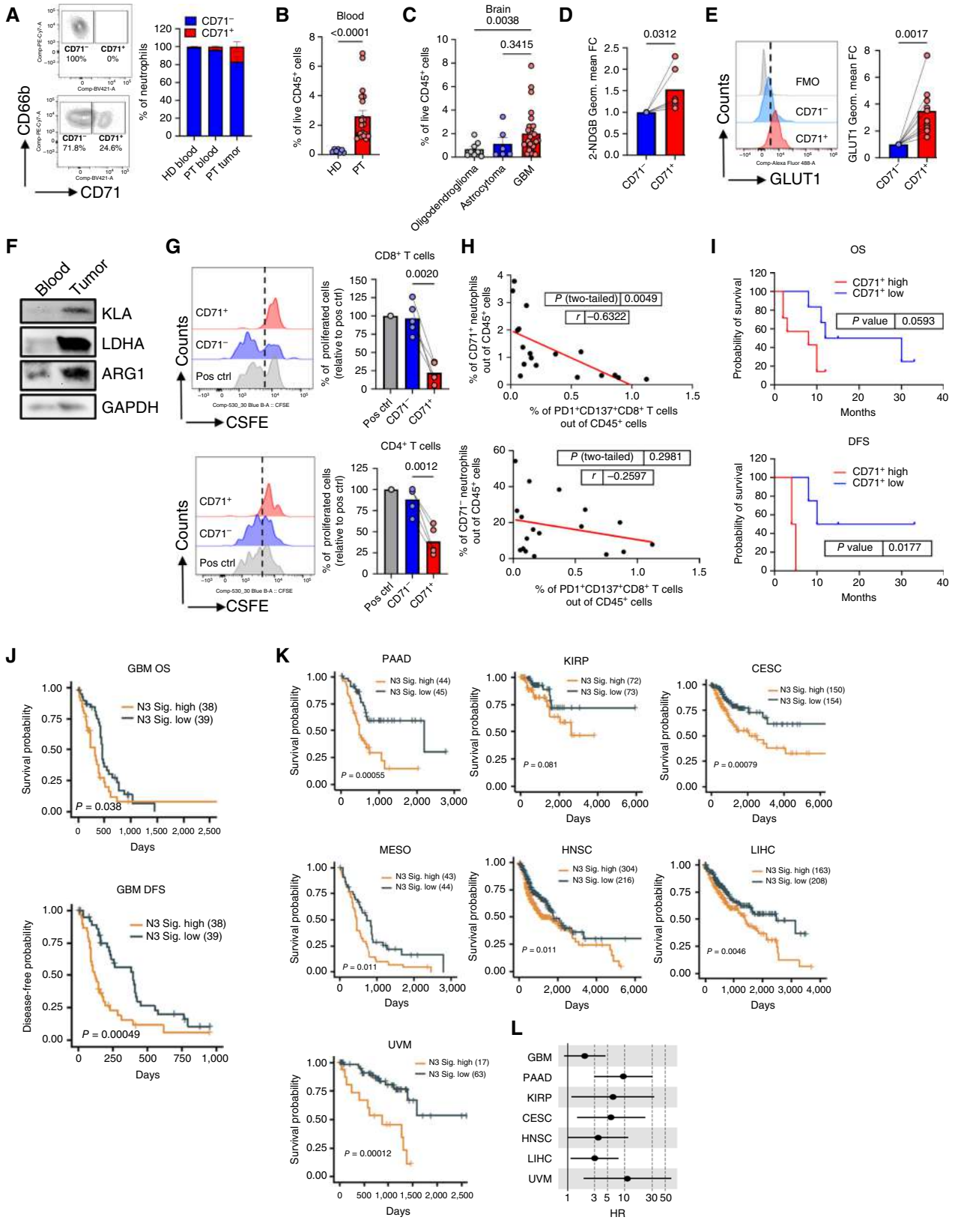

Figure 7. Human CD71⁺ neutrophils are immunosuppressive cells associated with reduced survival in different cancer types. **A,** Example of a human brain tumor–derived neutrophil gating strategy based on CD71 expression (left) and frequencies of CD71⁺ and CD71⁻ neutrophils in human blood and tumor (right), by FACS ($n = 7$). **B,** Frequency of CD71⁺ neutrophils out of live CD45⁺ cells in the blood of healthy donors (HD, $n = 7$) (*continued on following page*)

Hence, we treated mice with established brain tumors with isosafrole. Isosafrole treatment enhanced the survival of mice with brain tumors compared with mice treated with vehicle only (Fig. 6M). However, the combination of isosafrole with neutrophil depletion did not have an additive effect on mice survival (Supplementary Fig. S9G), suggesting that neutrophils are important mediators of the isosafrole-associated effects in brain tumors.

4-1BB agonism is considered an attractive strategy for the immunotherapy of cancer (40). However, as monotherapy, 4-1BB poorly prolonged the median survival of mice with brain tumors (15, 41). Thus, we next sought to determine whether isosafrole enhanced the activity of 4-1BB agonism. To test this hypothesis, we assessed the survival of mice with brain tumors (SB28) treated with the combination of isosafrole and anti–4-1BB. In combination with anti–4-1BB, isosafrole substantially delayed brain tumor progression in mice (Fig. 6M).

Together, our data identify Kla as a target to inhibit the function of immunosuppressive neutrophils within tumors and boost the efficacy of immunotherapy.

Human CD71$^+$ Neutrophils Show Immunosuppressive Features and Are Associated with Worse Outcomes in Multiple Human Cancers

To assess the relevance of our results to human disease, we analyzed the expression of CD71 in neutrophils from patients with brain tumors. Mirroring observations in mouse models, CD71 identified two different neutrophil subsets in human brain tumors (Fig. 7A). Although CD71$^+$ neutrophils represented about 20% of total neutrophils that infiltrated human GBM tumors, they represented 1% to 2% and 4% to 5% of total healthy donors' and patients' blood neutrophils, respectively (Fig. 7A). Moreover, we observed an expansion of CD71$^+$ neutrophils in the blood of patients with brain tumors compared with the peripheral blood of healthy donors (Fig. 7B). In parallel, we found that CD71$^+$ neutrophils were significantly more abundant in GBM tumors compared with oligodendrogliomas (Fig. 7C), which have a better prognosis. The infiltration of CD71$^+$ neutrophils was slightly higher in GBM compared with astrocytoma tumors (Fig. 7C). Of note, all astrocytoma tumors in this study were high-grade gliomas (grades 3–4, Supplementary Tables S1 and S2).

As observed in mice, we found that human tumor–infiltrating CD71$^+$ neutrophils demonstrated higher avidity for glucose (Fig. 7D), GLUT1 expression (Fig. 7E), as well as higher expression of glycolysis-associated genes, such as *ALDOC*, *LDHA*, and *PKM*, than CD71$^-$ neutrophils (Supplementary Fig. S10A). This glycolytic phenotype was accompanied by high levels of ARG1 (Supplementary Fig. S10B) and LOX1 (Supplementary Fig. S10C). As analyzing Kla in CD71$^+$ neutrophils by WB from patients' brain tumors was technically not possible due to the limited numbers of cells we could obtain, we analyzed Kla in total neutrophils isolated from brain tumors. Tumor-infiltrating neutrophils showed increased levels of Kla, LDHA, and ARG1 by WB compared with blood-derived neutrophils (Fig. 7F).

To clarify whether either ARG1 or LDHA inhibition affected the immunosuppressive ability of human CD71$^+$ neutrophils, we analyzed the suppressive ability of CD71$^+$ neutrophils generated from human CD34$^+$ hematopoietic stem cells with G-CSF + GM-CSF for 13 days and exposed to hypoxia (1% O_2) during the last 4 days of culture (Supplementary Fig. S10D). FACS-sorted neutrophils were cocultured with CFSE-stained CD3$^+$ T cells, stimulated with anti-CD3/anti-CD28 antibodies. By FACS, we found that CD71$^+$ neutrophils suppressed the proliferation of CD3$^+$ T cells. Either ARG1 (norNOHA) or LDHA (GNE140) inhibition fully abrogated the suppressive ability of CD71$^+$ neutrophils (Supplementary Fig. S10E). Our data suggest that ARG1 and LDHA are required for CD71$^+$ neutrophils to exploit their immunosuppressive activity in mouse and human neutrophils under hypoxic conditions.

We next analyzed the suppressive function of FACS-sorted CD71$^+$ neutrophils from human GBM tumors. Tumor-infiltrating CD71$^+$ neutrophils demonstrated a high ability to suppress the proliferation of CD4$^+$ and CD8$^+$ T cells (Fig. 7G). However, CD71$^+$ neutrophils isolated from the blood of the same patients with brain cancer lacked any suppressive ability (Supplementary Fig. S10F), confirming a functional reprogramming of CD71$^+$ neutrophils in the human GBM tumors. In addition, we found that the frequency of CD71$^+$ neutrophils,

Figure 7. ***(Continued)*** versus patients with brain cancer (PT, $n = 20$), by FACS. **C,** Frequency of CD71$^+$ neutrophils out of live CD45$^+$ cells in human brain cancers, based on the diagnosis. Oligodendroglioma $n = 8$, astrocytoma $n = 6$, GBM $n = 30$. **D,** 2-(N-(7-nitrobenz-2-oxa-1,3-diazol-4-yl)amino)-2-deoxyglucose (2-NDGB) uptake in human tumor–derived neutrophils, measured by FACS and expressed as Geometric mean FC to CD71$^-$ neutrophils ($n = 6$). **E,** GLUT1 expression in human tumor–derived neutrophils, measured by FACS and expressed as Geometric mean FC to CD71$^-$ neutrophils ($n = 10$). **F,** WB of indicated markers in human brain tumor–derived neutrophils ($n = 5$). **G,** Suppressive ability of human tumor–derived CD71$^+$ and CD71$^-$ neutrophils on CD8$^+$ (top) and CD4$^+$ (bottom) T-cell proliferation, measured as CFSE dilution by FACS ($n = 5$). **H,** Correlation between the frequencies of CD71$^+$ neutrophils (top) and CD71$^-$ neutrophils (bottom) and PD1$^+$CD137$^+$CD8$^+$ T cells out of CD45$^+$ cells in the tumor of patients with brain cancer by FACS ($n = 18$). **I,** Kaplan–Meier representation of the OS (top) or DFS (bottom) in our cohort of patients with GBM, based on the high (≥1.5% out of CD45$^+$ cells) or low (<1.5% out of CD45$^+$ cells) accumulation of CD71$^+$ neutrophils in the tumor, by FACS. High, $n = 7$; low, $n = 6$. **J,** N3 unique neutrophil gene signature association with patient OS (top) and DFS (bottom) in GBM cancer. Kaplan–Meier plots show OS and DFS for patients in the TCGA GBM cohort. Patients were split into high and low expression of the N3 signature (N3 Sig.) based on the optimal cutoff (see "Methods"). Events are represented by vertical lines and were defined as days to death (from initial pathologic diagnosis) or days to first event (from initial treatment and from clinical disease-free diagnosis). **K,** N3 unique neutrophil gene signature association with patients' OS in different solid human cancers. The optimal cutoff was used to separate patients into high versus low expression of the N3 signature. **L,** Forest plots show N3 signature HR scores associated with patient OS that were significant ($P < 0.05$) by Cox proportional hazards test. Dots indicate the calculated HR, and whiskers indicate 95% confidence intervals. All data are presented as mean ± SEM. Statistical analysis was performed using unpaired two-sided Student *t* tests (**B**), one-way ANOVA with Tukey's *post hoc* test (**C**), paired two-sided Student *t* tests (**D**, **E,** and **G**), Pearson correlation coefficient with the associated two-tailed *P* value (**H**), Kaplan–Meier method and log-rank test (**I**, **J**, and **K**), and Cox proportional hazards test (**L**). CESC, cervical squamous cell carcinoma and endocervical adenocarcinoma; GBM, glioblastoma; HNSC, head and neck squamous cell carcinoma; KIRP, kidney renal papillary cell carcinoma; LIHC, liver hepatocellular carcinoma; MESO, mesothelioma; PAAD, pancreatic adenocarcinoma; UVM, uveal melanoma.

but not of CD71⁻ neutrophils, negatively correlated with the presence of tumor-infiltrating CD8⁺PD1⁺CD137⁺ T cells (Fig. 7H; ref. 42), which are associated with an improved response to checkpoint blockade therapies in cancer (43–45). Consistently, a higher frequency of tumor-infiltrating CD71⁺ neutrophils by FACS was associated with poorer overall survival (OS) and disease-free survival (DFS) in our cohort of patients with GBM (Fig. 7I). Thus, our human data recapitulated the observations in mice.

Next, we hypothesized that the genetic signature of the N3 cluster might be predictive of clinical outcomes in patients with GBM. Of note, we established an N3 signature that is unique to this cluster of neutrophils and absent in other immune cells by comparing the N3 cluster with other immune cell types that were identified by performing scRNA-seq on total CD45⁺ cells from mouse brain tumors (Supplementary Table S3). To assess whether human neutrophils exhibit a transcriptomic signature that is analogous to the N3 cluster, we analyzed our mouse N3 signature in a published scRNA-seq of neutrophils from human pancreatic tumors (11). The N3 cluster was similar to a cluster of glycolytic neutrophils identified in human pancreatic tumors (Supplementary Fig. S10G). Indeed, the glycolytic TAN-1 cluster, found by Wang and colleagues (11), showed the highest enrichment of CD71⁺ signature genes (Supplementary Fig. S10H). Thus, intratumoral mouse and human neutrophils have an analogous transcriptomic signature. To test our hypothesis, we analyzed the OS and DFS in patients with GBM from TCGA by scoring patients based on low and high expression of the N3 signature. Patients with GBM who had a high N3 signature in tumor tissue had poorer OS and DFS compared with patients with GBM who had low expression of the N3 signature (Fig. 7J).

To assess whether the N3 signature might be applicable to a broader spectrum of human cancers, we compared OS with the expression of the N3 signature in human tumors using the TCGA database. We found that higher expression of the N3 signature was associated with poor OS across different common solid tumors (Fig. 7K and L; Supplementary Fig. S10I). Our data indicate that the N3 signature predicts poor clinical outcomes across human tumors.

DISCUSSION

Given the coexistence of different flavors of neutrophils with distinct functional phenotypes in tumor tissue, we interrogated how specific neutrophil subsets acquire immunosuppressive functionality within tumors. Our study shows that hypoxia-driven glucose metabolism reprograms the immunosuppressive function of a specific subset of neutrophils expressing CD71 via histone lactylation, which directly regulates the expression of ARG1 in these cells. A unique signature of immunosuppressive and glycolytic CD71⁺ neutrophils is associated with poor clinical outcomes across different human tumors.

Neutrophils demonstrated immunosuppressive functions in tumor tissue but not in peripheral organs/tissues. By scRNA-seq, we identified three main neutrophil clusters in mouse brain tumor tissue: hypoxic and glycolytic N3 expressing the transferrin receptor CD71 and N1 and N2 with enrichment in proinflammatory pathways. Our results are in line with previous studies showing that tumor tissue is mainly populated by three neutrophil clusters (7, 10). Because GLUT1 KO neutrophils lost their immunosuppressive activity in brain tumors (15) and N3 demonstrates enrichment in glycolysis and hypoxia, we reasoned that N3 might represent neutrophils with immunosuppressive activity. CD71 resolved neutrophil heterogeneity by distinguishing two main neutrophil subsets within brain tumors: CD71⁻ and CD71⁺. Tumor-infiltrating CD71⁺ neutrophils were potent immunosuppressive cells, experienced hypoxia, and demonstrated enhanced glucose metabolism, high avidity for glucose, and production of lactate, thus closely resembling the N3 cluster. CD71⁺ neutrophils were also detectable in the periphery, but as opposed to tumor-infiltrating CD71⁺ neutrophils, they lacked immunosuppressive properties.

On the other hand, CD71⁻ neutrophils, which were present in the periphery and tumor tissue along with CD71⁺ neutrophils, lacked immunosuppressive properties. As N1 and N2 clusters did not express CD71, they are most likely included in CD71⁻ neutrophils. N1 and N2 clusters also showed enrichment in proinflammatory and immune response–associated pathways; thus, they may have antitumor activity. This possibility is in line with previous studies showing the presence of antitumoral neutrophils in diverse cancer settings (9, 46–48). However, future studies will clarify the role of CD71⁻ neutrophils in brain tumors.

As immunosuppressive CD71⁺ neutrophils highly expressed ARG1, LOX1, CD14, VEGFα, TGFβ, and CXCR4, these cells are closely related to PMN-MDSCs (14). Depending on the setting, PMN-MDSCs are either mature or immature cells. Although CD71 was described as a marker of early neutrophil progenitors and immature neutrophils in human BM and in patients with cancer (21), CD71⁺ neutrophils were mostly mature cells in blood and tumors. PMN-MDSCs, which are virtually absent in tumor-free hosts, emerge from alterations in BM development programs during cancer progression (49) and are immunosuppressive cells in nontumor tissues with maximum activity in tumors (19, 49–51). CD71⁺ neutrophils are not suppressive cells in peripheral organs and are also present in naïve mice; thus, CD71⁺ neutrophils might not emerge from pathologic activation. Consistent with this possibility, we found that nonsuppressive CD71⁻ and CD71⁺ neutrophils are normally different from BM progenitors. On the other hand, the frequency of CD71⁺ neutrophils in blood and tumors increased during tumor progression, perhaps indicating pathologic myelopoiesis. As previous evidence showed that BM neutrophils in early-stage tumors are not suppressive but have features that distinguish them from BM neutrophils in tumor-free mice (52), we cannot exclude the possibility that systemically soluble factors released from tumors may condition CD71⁺ neutrophils in the BM or blood, facilitating their transition to immunosuppressive neutrophils when these cells migrate to the tumor tissues.

Hypoxia converted CD71⁺ neutrophils into suppressive cells but not CD71⁻ neutrophils, suggesting that CD71⁺ neutrophils may have cell-intrinsic features that favor their reprogramming into immunosuppressive cells. Importantly, soluble tumor-derived factors failed to induce immunosuppressive activity in CD71⁺ neutrophils, suggesting that the functional

reprogramming of CD71+ neutrophils requires very specific conditions. It was recently proposed that hypoxia was not required to trigger T3 subset reprogramming, and migration toward the hypoxic glycolytic niche occurred after the acquisition of T3 epigenetic and transcriptional programs, which can occur in normoxic conditions (10). Consistent with T3 neutrophil location, CD71+ neutrophils preferentially occupied hypoxic and glycolytic tumor niches. However, hypoxia is required for CD71+ neutrophil reprogramming into glycolytic cells with immunosuppressive activity. Although CD71+ neutrophil reprogramming does not occur in normoxic conditions and few CD71+ neutrophils were found in hypoxic "nonglycolytic niches," we cannot determine whether CD71+ neutrophils migrate toward hypoxic glycolytic niches either before or after their reprogramming. Such reprogramming of CD71+ neutrophils may allow these cells to exert their protumoral function and survive within hypoxic and glycolytic areas. Future investigations will clarify how neutrophils reach those areas as well as the functional consequences of this specific neutrophil positioning in the tumor tissue. As CD71+ neutrophils, but not CD71− neutrophils, acquire immunosuppressive activity upon exposure to the same tumor conditions, the capacity of neutrophils to adapt their specific functions in response to specific TME cues depends on the intrinsic features of these cells that determine their functional fate once within a tumor. As hypoxic neutrophils suppress T-cell proliferation in normoxic conditions, the hypoxic and glycolytic phenotype with suppressive functionality is a terminal functional state that might not be reverted. Thus, we propose that targeting mechanisms that drive the reprogramming of neutrophils into immunosuppressive cells would be more effective than attempting to revert their function in tumors.

The proportion of CD71+ neutrophils in total neutrophils within tumors was higher than in the periphery, indicating that they may stem from CD71− neutrophils that infiltrated tumors. However, we argue that CD71− neutrophils give rise to CD71+ neutrophils because either hypoxia or tumor-derived factors generate immunosuppressive CD71+ neutrophils from CD71− neutrophils. Consistently, both neutrophil subsets appeared at early time points during neutrophil differentiation from proNeu, suggesting that both subsets may directly derive from proNeu. Future studies will clarify this point.

CD71+ neutrophils were long-lived cells in the TME. This is in line with recent studies showing that protumoral neutrophils have prolonged survival in tumors (10, 12). Consistently, the expression of CXCR4 (53–55) and GLUT1 (24), as markers of aging, further suggests that intratumoral CD71+ neutrophils persist longer in tumors. CD71+ neutrophils expressed higher levels of CXCR4 in blood and tumors; thus, CXCR4 may support CD71+ neutrophil colonization of brain tumors from the periphery. In line with this hypothesis, a recent study demonstrated that CXCR4 promoted the accumulation of neutrophils in inflamed tissues without affecting their homeostatic migration into naive tissues (56, 57). Consistently, BM-derived cells were recruited to tumors in part through the interaction of CXCL12 and its receptor, CXCR4, in which overexpression in brain tumors correlated with tumor grade and poor prognosis (58, 59). Thus, CXCR4 may favor the migration of CD71+ neutrophils in GBM tumors, in which they are reprogrammed into immunosuppressive cells.

Neutrophils undergo a profound metabolic adaptation within tumors, ultimately leading to the adoption of a protumoral phenotype. CD71+ neutrophils were intrinsically more glycolytic than CD71− neutrophils, suggesting different metabolic demands by distinct neutrophil subsets. Hypoxia-driven glucose metabolism was required for the induction of immunosuppressive activity by CD71+ neutrophils. Consistently, GLUT1 affects the ability of neutrophils to suppress the proliferation of T cells. In line with a protumoral role for glycolytic neutrophils, proangiogenic neutrophils are found in hypoxic and glycolytic regions of pancreatic tumors (10, 11). In our study, we linked, for the first time, glucose metabolism to the suppressive ability of neutrophils. Importantly, CD71− and CD71+ neutrophils showed similar OCR, suggesting that oxidative metabolism might not be required for the induction of suppressive functions by CD71+ neutrophils. Glucose was utilized to generate high amounts of lactate that regulated the expression of ARG1 via Kla. Similarly to what we previously observed in MDM (15), intracellular lactate was largely used for Kla. In fact, the inhibition of extracellular lactate uptake did not inhibit histone lactylation or the immunosuppressive ability of neutrophils. Accordingly, the inhibition of glucose metabolism, lactate production, or the Kla writer (CBP/p300) fully abrogated Kla and consequently the ARG1-driven immunosuppressive function of neutrophils. Previous evidence shows that Kac is required for the acquisition of protumoral properties by myeloid cells (36, 60). We found that the functional reprogramming of CD71+ neutrophils did not require Kac. Indeed, CD71− and CD71+ neutrophils showed low but similar levels of Kac. Hypoxia boosted Kla, but not Kac, in CD71+ neutrophils. Moreover, the inhibition of ACLY that generates acetyl–CoA as a substrate for Kac failed to alter the function of CD71+ neutrophils. In support of our results, a recent study demonstrated that Kac is required for the antitumor potential of neutrophils (9).

We defined a unique signature of N3 neutrophils that predicted poor OS and DFS in patients with GBM, as well as OS in a broad collection of other human cancers, indicating that this signature is conserved across tumors and species. This result highlights the negative role of specific neutrophil subsets and the intrinsic capacity of certain neutrophil subsets to be reprogrammed into suppressive cells in cancer.

In summary, our study suggests a novel mechanism by which hypoxia-driven histone lactylation regulates the immunosuppressive functions of specific subsets of tumor-infiltrating neutrophils, opening the possibility to target specific immunosuppressive neutrophils in GBM and in cancer settings beyond brain tumors.

METHODS

Human Samples

Samples of peripheral blood and tumor tissues were collected from patients at Moffitt Cancer Center (MCC; Tampa, Florida) and at the Department of Neurology and Neurosurgery at Policlinico Umberto I Hospital (Rome, Italy). The study was approved by the MCC Institutional Review Board, and all patients signed a written informed consent that was approved by the Institutional Review Board. Samples collected at the Department of Neurology and Neurosurgery at Policlinico Umberto I Hospital (Rome, Italy) were

collected in accordance with the Declaration of Helsinki and with good clinical practice guidelines, and all patients signed a written informed consent (Policlinico Umberto I Ethics Committee Protocol, RIF.CE: 4181). Blood and tissue specimens were immediately collected from the operating room and processed as described below.

Clinical Sample Processing

Freshly resected human brain tissue samples were taken to the laboratory within 2 hours to start tissue dissection and processing. Tissue specimens were washed in 1X PBS and macrodissected under sterile conditions. They were further processed with the Tumor Dissociation Kit (Miltenyi), according to the manufacturer's instructions, using the gentleMACS Dissociator (Miltenyi). Afterward, the homogenate was filtered through a 70-μm cell strainer and centrifuged at 400 × *g* for 8 minutes at 4°C to pellet the cells and myelin. This was followed by a myelin removal step using gradient centrifugation with 30% Percoll (Sigma-Aldrich) in 1X PBS (1,592 × *g* for 30 minutes at 4°C; with slow acceleration and without breaks during deceleration). After myelin (the top white layer) removal, the middle transparent layer and the single-cell suspension were washed in 1X PBS and centrifuged at 400 × *g* for 8 minutes at 4°C to pellet the cells. The cells were then used for downstream analysis. Peripheral blood mononuclear cells were obtained from blood after Percoll gradient stratification for 20 minutes at 2,000 RPM at room temperature (RT) without a break.

Cell Lines

GL261 and SB28 cells were obtained from the NCI and Hideho Okada at the University of California, respectively. They were cultured in RPMI (Gibco) supplemented with 10% FBS (Gibco), 1% penicillin/streptomycin (Gibco), and 55 μmol/L 2-mercaptoethanol (Gibco). Tumor cell lines tested negative for mycoplasma contamination.

Mouse Models

Animal experiments were approved by the H. Lee MCC and by the Wistar Institutional Animal Care and Use Committee. C57BL/6 mice (female/male, 6–8 weeks old) were purchased from The Jackson Laboratory (RRID:IMSR_JAX:000664). *Slc2a1*$^{fl/fl}$ *Lyz2-Cre* mice were created after breeding *Slc2a1*$^{fl/fl}$ (Slc2a1tm1.1Stma, RRID:IMSR_JAX:031871) mice with *Lyz2-Cre* [B6.129P2-Lyz2tm1(cre)Ifo/J, RRID:IMSR_JAX:004781]. *Lyz2-Cre* [B6.129P2-Lyz2tm1(cre)Ifo/J] mice were obtained from Paulo Rodriguez at MCC. *Slc2a1*$^{fl/fl}$ (Slc2a1tm1.1Stma) mice were obtained from The Jackson Laboratory. *Tfrc*$^{fl/fl}$ S100A8-cre mice were created after breeding *Tfrc*$^{fl/fl}$ [B6.129S(Cg)-Tfrc<tm3.1Nca>/J, RRID:IMSR_JAX:028363] mice with S100A8-cre [B6.Cg-Tg(S100A8-cre,-EGFP)1Ilw/J, RRID:IMSR_JAX:021614] mice. Both *Tfrc*$^{fl/fl}$ [B6.129S(Cg)-Tfrc<tm3.1Nca>/J] mice and S100A8-cre [B6.Cg-Tg(S100A8-cre,-EGFP)1Ilw/J] mice were obtained from The Jackson Laboratory.

Orthotopic Glioma Cell Injection

Mice were intracranially injected with GL261 (40,000 cells) or SB28 (10,000 cells) into the right posterior cortex (1.5 mm posterior to bregma, 1.5 mm lateral to bregma, and 2.5 mm deep) using a stereotactic apparatus. Mice were monitored daily for neurologic symptoms, lethargy, and hunched posture that would qualify as signs of tumor burden.

Processing of Mouse Brain Samples

Mice were euthanized with CO_2 and perfused with 20 mL of 1X PBS through the left ventricle of the heart using a 25-G needle attached to a 50-mL syringe. Brain tumor tissues were washed in 1X PBS, macrodissected under sterile conditions, and further processed with the Tumor Dissociation Kit (Miltenyi), according to the manufacturer's instructions, using the gentleMACS Dissociator (Miltenyi). Afterward, the homogenate was filtered through a 70-μm cell strainer and centrifuged at 400 × *g* for 8 minutes at 4°C to pellet the cells and myelin. This was followed by a myelin removal step using gradient centrifugation with 30% Percoll (Sigma-Aldrich) in 1X PBS (1,592 × *g* for 30 minutes at 4°C; with slow acceleration and without breaks during deceleration). After myelin (the top white layer) removal, the middle transparent layer and the single-cell suspension were washed in cold PBS and centrifuged at 400 × *g* for 8 minutes at 4°C to pellet the cells. The cells were counted and then used for downstream analysis.

FACS-Sorting

Cells were incubated with a cocktail of surface antibodies, Fc Block (BD Biosciences), and Aqua Fixable viability dye (Invitrogen) in FACS buffer (1X PBS, 1% FBS, 0.5 mmol/L EDTA) at RT for 30 minutes. Afterward, cells were washed with FACS buffer and filtered with a 70-μm cell strainer, and then, target cells were sorted using FACSAria II (BD Biosciences) using FACSDiva (BD Biosciences, RRID:SCR_001456).

Surface and Intracellular Staining for Flow Cytometry

For surface staining, 0.5 × 10^6 cells were incubated with a cocktail of surface antibodies, Fc Block (BD Biosciences), and Aqua Fixable viability dye in FACS buffer at RT for 30 minutes. For intracellular staining, cells were fixed and permeabilized with fixation/permeabilization buffers (BD Biosciences) at 4°C for 15 minutes, washed twice with wash buffer (BD Biosciences), and incubated with a cocktail of intracellular antibodies at 4°C for 30 minutes. Cells were run on either a BD FACSymphony (BD Biosciences) or a BD LSRII (BD Biosciences), and data were analyzed using FlowJo (Tristar, RRID:SCR_008520). Surface and intracellular stainings were performed with the following anti-mouse antibodies: anti-PIMO (Hypoxyprobe), anti-rabbit AF647 (Invitrogen, A21244), CD101 PE-Cy7 (Invitrogen, 25-1011-80), CD103 BV421 (BioLegend, 121422), CD103 BV711 (BD Biosciences, 748255), CD115 PE/Dazzle 594 (BioLegend, 135527), CD117 (cKit) BV786 (BD Biosciences, 564012), CD11b BUV805 (BD Biosciences, 741934), CD11b APC-Cy7 (BioLegend, 101226), CD11C AF647 (BioLegend, 117312), CD135 (FLT3) BV421 (BioLegend, 135315), CD137 PE (BioLegend, 106105), CD137 APC (BioLegend, 106110), CD14 BV421 (BioLegend, 123329), CD14 BV785 (BioLegend, 123337), CD16/32 (BV711; BD Biosciences, 740659), CD170 (Siglec-F) APC (BioLegend, 155507), CD3 FITC (BioLegend, 100306), CD3 PE-Cy5 (BD Biosciences, 553065), CD3 APC (BioLegend, 100236), CD34 PE (BD Biosciences, 551387), CD4 PerCP/Cy5.5 (BioLegend, 100434), CD4 BUV496 (BD Biosciences, 612952), CD45 PerCP/Cy5.5 (BioLegend, 103132), CD45 (AF700; BioLegend, 103128), CD45.1 PE (BioLegend, 110707), CD45.2 AF700 (BioLegend, 109821), CD45R (B220) AF488 (BioLegend, 103225), CD45R/B220 APC-Cy7 (BD Biosciences, 552094), CD49d AF488 (BioLegend, 103611), CD49d PE/Dazzle 594 (BioLegend, 103625), CD71 BV421 (BioLegend, 113813), CD71 APC (Invitrogen, 17-0711-82), CD81 PE-Cy7 (BioLegend, 104913), CD8a BV750 (BD Biosciences, 747134), CD8a BUV737 (BD Biosciences, 612759), CD8a PE (BioLegend, 100708), CD90.2 FITC (BioLegend, 140303), MHC Class II (I-Ab) PE-Cy7 (BioLegend, 116420), CXCR2 PE (BioLegend, 149303), CXCR2 APC-Cy7 (BioLegend, 149313), CXCR4 APC (BioLegend, 146507), DcTRAIL-R1 (PE, BioLegend, 133804), F4/80 PE (BioLegend, 123110), Fc Block (TruStain FcX; BioLegend, 101320), GLUT-1 PE-Cy5.5 (Novus Biologicals, NB110-39113), IFNγ PE (BioLegend, 505808), LY6C BV605 (BD Biosciences, 563011), LY6C APC (BD Biosciences, 560595), Ly6G PE-Cy7 (BioLegend, 127618), Ly6G BUV563 (BD Biosciences, 612921), NK-1.1 BUV661 (BD Biosciences, 741477), PD-L1 (CD274) BV650 (BioLegend, 124336), PD-L1 (CD274) PE-Cy7 (BioLegend, 124314), and Sca-1 (LY6A/E) PerCP/Cy5.5

(BioLegend, 108124), and the following anti-human antibodies: CCR2 PE (BioLegend, 357205), CD11b BB700 (BD Biosciences, 742210), CD11b APC (BioLegend, 301350), CD11c AF647 (BioLegend, 301622), CD137 (4-1BB) BUV496 (BD Biosciences, 7416420), CD14 APC-Cy7 (BioLegend, 367108), CD15 PerCP/Cy5.5 (BioLegend, 301922), CD16 PE (BioLegend, 302008), CD3 BUV805 (BD Biosciences, 741999), CD3 PE (BioLegend, 300308), CD4 PE-Cy5 (BD Biosciences, 566925), CD4 AF647 (BioLegend, 300520), CD45 AF700 (BioLegend, 368514), CD49D BV605 (BioLegend, 304324), CD49D AF647 (BioLegend, 304335), CD56 BUV737 (BD Biosciences, 741842), CD66b PE-Cy7 (BioLegend, 305116), CD66b PE/Dazzle 594 (BioLegend, 305121), CD71 BV421 (BioLegend, 334122), CD8 BV650 (BD Biosciences, 740587), CD8 AF488 (BioLegend, 301021), CX3CR1 FITC (BioLegend, 341606), FcR Blocking (Miltenyi, 130-059-901), GLUT-1 AF488 (R&D Systems, FAD1418G), HLA-DR BV785 (BioLegend, 307641), HLA-DR FITC (BioLegend, 307604), LOX1 PE (BioLegend, 358604), LOX1 APC (BioLegend, 358605), P2RY12 FITC (BioLegend, 392107), P2RY12 PE/Dazzle 594 (BioLegend, 392112), PD-1 BUV395 (BD Biosciences, 745619), and PD-L1 BV785 (BioLegend, 329735).

Glucose Uptake

Cells were incubated with PBS containing 40 μmol/L fluorescent D-glucose analog 2-2-[N-(7-nitrobenz-2-oxa-1,3-diazol-4-yl) amino]-2-deoxy D-glucose (catalog N13195, Life Technologies) for 40 minutes at 37°C. Cells were then washed with cold MACS buffer, stained with surface antibodies for 30 minutes at 4°C, and washed again with cold MACS buffer, and fluorescence intensities were immediately analyzed by flow cytometry.

Processing Neutrophils for scRNA-Seq

Mice were injected with 10,000 SB28 cells. After 18 days, neutrophils were sorted from tumor and blood. Blood was collected by submandibular puncture followed by cardiac puncture (right atrium). After blood collection, mice were perfused with 20 mL of 1X PBS through the left ventricle, and the tumor was collected and processed as previously described. Neutrophils were then FACS-sorted in MACS buffer, as previously described. After sorting, neutrophils were washed in RPMI containing 10% FBS and 1 U/μL of Protector RNase Inhibitor (Sigma, PN-3335399001). The media were filtered through 0.22 μm before use. Cells were then counted and resuspended at a concentration of 1,000 cells/μL. A total of 20,000 cells per lane were loaded for encapsulation. Cells were then processed with 10X Chromium 3′ scRNA-seq, 40,000 reads/cell, using NovaSeq S1-100 and NovaSeq SP-100 sequencing runs.

Western Blot

Cells were lysed in RIPA buffer (Cell Signaling Technology) in the presence of a protease and phosphatase inhibitor cocktail (Thermo Fisher Scientific), 1 mmol/L dithiothreitol (DTT), sodium butyrate (1:100), and 1 mmol/L phenylmethylsulfonyl fluoride (PMSF); sonicated; and stored at −80°C. Whole-cell lysates were prepared and subjected to SDS–PAGE and transferred to a polyvinylidene difluoride (PVDF) membrane. The membranes were probed overnight at 4°C with primary antibodies. Membranes were washed and incubated for 1 hour at RT with a secondary antibody conjugated with peroxidase. Blots were developed with enhanced chemiluminescence (Millipore), and signals were captured with the Odyssey Fc (LI-COR). Membranes were incubated with the following primary and secondary anti-mouse/anti-human antibodies: ARG1 (BD Biosciences, Cat#610709), HIF-1α (Cell Signaling Technology, Cat#36169S), vinculin (7F9, Santa Cruz Biotechnology, Cat#sc-73614), β-actin (13E5, Cell Signaling Technology, Cat#5125), L-lactyllysine (PTM BIO, Cat#PTM-1401RM), acetyllysine (PTM BIO, Cat#PTM-101), histone 3 (PTM BIO, Cat#PTM-1002RM), Lamin A/C (4C11, Cell Signaling Technology, Cat#4777), GLUT1 (Novus Biologicals, NB110–39113SS), LDHA (R&D, AF7304), inducible nitric oxide synthase (BD Biosciences, 610432), transferrin receptor (Invitrogen, 13-6800), β-tubulin (Cell Signaling Technology, 86298T), anti-mouse IgG [horseradish peroxidase (HRP)–conjugated, Bio-Rad, 1706516], anti-rat IgG (HRP-conjugated, R&D Systems, HAF005), anti-sheep IgG (HRP-conjugated, R&D Systems, HAF016), anti-MCT1 (Novus Biologicals, NBP1-59656SS), and anti-MCT2 (Alomone Labs, AMT-012).

CUT&RUN

A diluted aliquot of cell suspension was mixed with trypan blue (1:1) and counted on a hemocytometer. Equal numbers of cells were pooled and diluted to a final concentration of 1,000 to 300 cells/μL in wash buffer, with 100 μL (~100,000 cells for *in vitro* experiments and ~30,000 cells for *in vivo* experiments) used for each CUT&RUN reaction. CUT&RUN was performed using the CUT&RUN Assay Kit (Cell Signaling Technology) according to the manufacturer's instructions. The DNA was immunoprecipitated with pan-Kla antibody (PTM1401RM, PTM BIO) or IgG as a nonspecific control. The precipitated chromatin DNA was purified using a DNA Clean & Concentrator-5 kit (Zymo Research) and detected by qRT-PCR using specific primers.

Preparation of Tumor Explant Supernatant

Tumor explant supernatants (TES) were prepared from excised mouse and human tumors. A small tumor piece (5–10 mm^2) was minced into pieces less than 3 mm in diameter and resuspended in 15 to 20 mL of RPMI without FBS but supplemented with 1% penicillin/streptomycin. After 16 to 18 hours of incubation at 37°C with 5% CO_2, the cell-free supernatant was collected, passed through 0.22-μm filters, and stored at −80°C.

qRT-PCR

RNA was extracted using the Quick-RNA Microprep Kit (Zymo Research) according to the manufacturer's instructions. RNA was DNase-treated and converted to random-primed cDNA using the SuperScript IV kit (Invitrogen). cDNA was used as a template in subsequent PCR with gene-specific primers (Supplementary Table S4). qRT-PCR was performed using Power SYBR Green PCR Master Mix (Applied Biosystems) in 96- or 384-well plates. Plates were read with the ABI 7900 (Applied Biosystems).

Seahorse Analysis

OCR and extracellular acidification rate were measured using an XF96 extracellular flux analyzer (Agilent) through mitochondrial and glycolysis stress tests. Cells were plated onto Cell-Tak precoated wells (1×10^5 cells/well in triplicate) and subjected to mitochondrial stress and glycolysis stress protocols using specific nonbuffered XF base media (Agilent). For the mitochondrial stress test, cells were analyzed under basal conditions and in response to 1 μmol/L oligomycin, 2 μmol/L fluorocarbonyl-cyanide-phenylhydrazone, and 0.5 μmol/L rotenone/antimycin A. For the glycolysis stress test, cells were plated in XF media lacking glucose and pyruvate and monitored under basal conditions and in response to 10 mmol/L glucose, 1 μmol/L oligomycin, and 50 mmol/L 2-DG.

Lactate Colorimetric Assay

Intracellular lactate concentrations were assessed using a Lactate Colorimetric Assay Kit II (Sigma).

Pimonidazole Staining

Hypoxyprobe-1 (pimonidazole hydrochloride) solution was injected intraperitoneally at a dosage of 60 mg/kg. One hour after injection, mice were euthanized, and tissues were collected. After tissue

processing, single-cell suspensions were stained for surface antigens and subsequently processed for intracellular staining. A purified rabbit anti-PIMO (Pab2627AP) was used at a 1:50 dilution (60 minutes at RT) for the intracellular staining, followed by a secondary APC-conjugated anti-rabbit staining (30 minutes at RT).

Isolation of Murine and Human Neutrophils

To obtain mature neutrophils, femurs and tibiae of naïve C57BL/6 mice (female/male, 6–8 weeks old) were flushed with MACS buffer; BM cells were then filtered through a 70-μm cell strainer, and red blood cells were lysed with the ACK lysing buffer. Neutrophils were obtained from single-cell suspensions by positive selection with anti-Ly6G microbeads; purity was checked by FACS (only samples containing >95% of neutrophils were used for further experiments). For human blood neutrophils, 15 mL of Histopaque-1119 was added to a 50-mL tube, followed by 15 mL of Histopaque-1077; then, 15 mL of blood was carefully added on top. The tube was centrifuged for 30 minutes at 872 × *g* and 4°C with no break. The bottom white layer was collected and stained with an anti-CD66b to check purity (only samples containing >95% neutrophils were used for further experiments). In some experiments, isolated murine and human neutrophils were treated with hypoxia or TES 30% for 24 to 48 hours.

Differentiation of Neutrophils from BM Cells

To generate *in vitro* $CD71^-$ neutrophils and $CD71^+$ neutrophils, BM cells were cultured for 6 days with GM-CSF. Briefly, the femur and tibiae of naïve C57BL/6 mice (female/male, 6–8 weeks old) were flushed with cold FACS buffer; BM cells were then filtered through a 70-μm cell strainer, and red blood cells were lysed with the ACK lysing buffer. Cells were seeded at a concentration of 3×10^5 cells/mL in six-well plates, 3 mL/well, with 20 ng/mL of GM-CSF (PeproTech) on day 0 in normoxic conditions. On day 3, GM-CSF was added to the culture in 1 mL of fresh complete RPMI, and part of the cells were moved to the hypoxia chamber. Hypoxic conditions were maintained by generating 1% O_2 and 5% CO_2 concentrations through the BioSpherix subchamber system, which includes a C-Chamber and ProOx C21 Oxygen CO_2 Single Chamber Controller. In TES experiments, 30% of TES was added to the cultures on day 3. In some experiments, cells were treated with 5 mmol/L 2-DG on day 5, LDHA inhibitor (GNE-140) 10 μmol/L on day 3 and 5 μmol/L on days 4 and 5, ACLY inhibitor (BMS-303141) 20 μmol/L on days 3, 4, and 5, CPI1612 25 nmol/L on days 4 and 5 (for CUT&RUN experiments, CPI1612 10 nmol/L was added only for the last 4 hours of culture), AZD3965 10 μmol/L on day 3, and isosafrole (Chem Service) 250 μmol/L on day 3.

Suppression Assay

FACS-sorted neutrophils (neutophils to T cells ratio 1:1) were cocultured with splenic autologous $CD3^+$ T cells isolated with the MojoSort Mouse CD3 T Cell Isolation Kit (BioLegend) and prestained with CFSE in a U-bottom, 96-well plate bound with anti-CD3 and anti-CD28 (1 μg/mL each, eBioscience) for 3 days. In some experiments, neutrophils were cocultured with CFSE-labeled T cells in the presence of norNOHA (Millipore, 750 μmol/L). For IFNγ production experiments, 66 hours after plating the cells, the cells were restimulated with the cell activation cocktail containing phorbol 12-myristate 13-acetate (PMA) and ionomycin (BioLegend) at a concentration of 2 μL/mL and with GolgiStop (BD Biosciences) at a concentration of 0.6 μL/mL for 6 hours. Cells were first stained for surface antigens and then fixed/permeabilized for intracellular staining and stained with PE anti–IFNγ (1:100) for 30 minutes at 4°C. IFNγ production was analyzed by FACS. FACS-sorted human neutrophils (neutophils to T cells ratio 1:1) were cocultured with negatively selected splenic autologous $CD3^+$ T cells isolated from the same donor using the MojoSort Human CD3 T Cell Isolation Kit (BioLegend) and prestained with CFSE in U-bottom, 96-well plates coated with anti-CD3 (clone UCHT1; BD Biosciences) at a final concentration of 20 μg/mL in sterile PBS (clone UCHT1; BD Biosciences). Two micrograms per milliliter (fresh complete RPMI) of soluble anti-CD28 (clone CD28.2; BD Biosciences) was added to the coculture. T-cell proliferation was evaluated after 3 days by FACS. For T-cell isolation, peripheral blood mononuclear cells from the same donor as the neutrophils were collected from whole blood, and T cells were isolated using the Human $CD3^+$ T Cell Enrichment Column Kit (R&D Systems), stained with CFSE, and resuspended in fresh complete RPMI containing 10% FBS and penicillin/streptomycin (1:100). Neutrophils' suppressive ability was analyzed as the neutrophils' ability to inhibit T-cell proliferation compared with T cells alone (positive control).

Mini Suppression Assay

For both mouse and human *ex vivo* mini-suppression assays, neutrophils were sorted in FACS buffer, washed in complete RPMI, and counted. Neutrophils were resuspended at a concentration as low as 5,000 cells/50 μL (between 5,000 and 25,000 cells in 50 μL). CFSE-prestained T cells were resuspended at the same concentration as neutrophils and used for the mini-suppression assay at a 1:1 ratio, in a final volume per well of 100 μL (50 μL of neutrophils and 50 μL of T cells).

Giemsa Staining

Sorted neutrophils were cytospinned onto glass microscope slides. The slides were fixed in methanol for 5 to 7 minutes. Giemsa stain was diluted 1:20 with deionized water. The slides were stained for 45 minutes and rinsed three times with deionized water, and a coverslip was mounted with CytoSeal 60 mounting media.

3-(4,5-dimethylthiazol-2-yl)-2,5-diphenyltetrazolium bromide (MTT) Assay

SB28 cells were plated at a density of 2.5×10^3 cells per well in 100 μL of complete media and were allowed to attach. After 8 hours, either isosafrole (250 μmol/L) or DMSO was added in 100 μL of complete media. For the positive control, 100 μL of complete media was added; for the negative control, 100 μL of H_2O was added. After 72 hours, viability was assessed with the RealTime-Glo MT Cell Viability Assay (Promega, G9711) following the manufacturer's instructions.

Isotope Tracing Experiments

Neutrophils were differentiated as described above. Neutrophils were switched to RPMI no-glucose media (Gibco) and supplemented with 25 mmol/L of U-$^{13}C_6$ D-glucose (Cambridge Isotope Laboratories) for 48 hours. Cells were lysed in denaturing lysis buffer containing 8 mol/L urea, 20 mmol/L HEPES (pH 8), 1 mmol/L sodium orthovanadate, 2.5 mmol/L sodium pyrophosphate, and 1 mM β-glycerophosphate. The proteins were reduced with 4.5 mmol/L DTT and alkylated with 10 mmol/L iodoacetamide. Trypsin digestion was carried out at RT overnight, and tryptic peptides were then acidified with 1% trifluoroacetic acid and desalted with C18 Sep-Pak cartridges according to the manufacturer's procedure (60108-390, Thermo Fisher Scientific). The peptides were then frozen on dry ice before lyophilization. Following lyophilization, the dried peptide pellet was redissolved in IP buffer containing 100 mmol/L NaCl, 1 mmol/L EDTA, 20 mmol/L Tris-HCl, and 0.5% NP-40 (pH 8.0). Lactylated lysine–containing peptides were immunoprecipitated with immobilized anti–lactyl lysine (Lac-K) antibody (PTM-1404, PTM BIO). The lactyl lysine–containing peptides were eluted with aqueous 0.1% trifluoroacetic acid. The eluted lactylated peptides were dried and redissolved in aqueous 2% acetonitrile containing 0.1% formic acid. A nanoflow ultrahigh-performance liquid chromatograph (Thermo Fisher Scientific) interfaced with an electrospray benchtop

quadrupole-orbitrap mass spectrometer (Orbitrap Exploris 480 with field asymmetric waveform ion mobility spectrometry, Thermo Fisher Scientific) was used for LC/MS-MS peptide sequencing experiments. The sample was first loaded onto a precolumn (C18 PepMap100, 100 µm Inner Diameter (ID) × 2 cm length packed with C18 reversed-phase resin, 5 µm particle size, 100 Å pore size) and washed for 8 minutes with aqueous 2% acetonitrile containing 0.04% trifluoroacetic acid. The trapped peptides were eluted onto the analytic column (C18 PepMap100, 75 µm ID × 25 cm length, 2 µm particle size, 100 Å pore size, Thermo Fisher Scientific). The 120-minute gradient was programmed as follows: 95% solvent A (aqueous 2% acetonitrile + 0.1% formic acid) for 8 minutes, solvent B (90% acetonitrile + 0.1% formic acid) from 5% to 38.5% in 90 minutes, then solvent B from 50% to 90% B in 7 minutes and held at 90% for 5 minutes, followed by solvent B from 90% to 5% in 1 minute and re-equilibration for 10 minutes. The flow rate on the analytic column was 300 nL/minute. Spray voltage was 2,100 V. Capillary temperature was set at 300°C. For high field asymmetric waveform ion mobility spectrometry, two compensation voltage values were applied: −45 and −65. Data-dependent scans were performed following each survey scan using a 15-second exclusion for previously sampled peptide peaks for a 1.5-second cycle time before the next MS survey scan. MS and MS-MS resolution were set at 120,000 and 45,000, respectively. Database searches were performed with MaxQuant (version 1.6.14.0) against the Swiss-Prot mouse database (version 2023_01) with parameters set for full trypsin, allowing up to two missed cleavages. Oxidized Methylated and lactylated lysine were set as variable modifications, and carbamidomethyl cysteine was set as a fixed modification. Mass tolerances were set at 4.5 ppm for MS1 and 20 ppm for MS2, and protein identifications with a minimum of one peptide were filtered at 5% FDR at the peptide spectrum matches (PSM) and peptide levels. The raw data were normalized per million cells processed.

In Vivo Treatments

A total of 10,000 SB28 cells were injected intracranially. For neutrophil depletion, we performed i.p. injections of a rat anti-Ly6G antibody (BE0075-1, 200 µg/mouse) combined with an anti-rat antibody (BE0122, 50 µg/mouse; ref. 17) every other day starting on day 7 after brain tumor initiation. Control mice were treated with the corresponding isotype control (BE0089, 200 µg/mouse) combined with an anti-rat antibody (BE0122, 50 µg/mouse). Neutrophil depletion was checked in blood on day 11 and in blood and tumor on day 16, and treatment was stopped at the experimental endpoint. For evaluation of the immune cell landscape in tumor tissue, mice were euthanized on day 14, following neutrophil depletion treatment. Tumors were collected and weighed. Tumors of similar sizes were processed to obtain single-cell suspensions and then stained for surface markers. CountBright Absolute Counting Beads (Invitrogen, C36950) were used to count cells by flow cytometry. Isosafrole (Chem Service, N-12281) was administered intraperitoneally in 200 µL of 1% carboxymethylcellulose (prepared in saline solution; 200 mg/kg) every other day starting from day 7. For the ARG1 inhibitor norNOHA, SB28-bearing mice were treated for 3 days (starting from day 15) with 100 mg/kg of norNOHA in 100 µL of 1X PBS intraperitoneally once per day. The respective vehicles were used as controls for each experiment.

scRNA-Seq Data Processing, Filtering, Batch Effect Correction, and Clustering

Raw sequencing reads from scRNA-seq were processed using Cell Ranger (version 5.0, 10x Genomics). Briefly, the base call files generated by Illumina sequencers were demultiplexed into fastq files based on the sequences of the sample index and aligned against the GRCm38 mouse transcriptome using STAR (61). Cell barcodes and Unique Molecular Identifiers (UMIs) associated with the aligned reads were subjected to correction and filtering. Filtered gene-barcode matrices containing only barcodes with UMI counts passing the threshold for cell detection were imported to Seurat version 4.0 (62) for downstream analysis. Barcodes with fewer than 200 genes expressed or more than 10% of UMIs originating from mitochondrial genes were filtered out; genes expressed in fewer than three barcodes were also excluded. For each sample, standard library size and log-normalization were performed on raw UMI counts using NormalizeData(), and the top 5,000 most variable genes were identified by the "vst" method in FindVariableFeatures(). The scaled *z*-scores for each gene were calculated using the ScaleData() function in Seurat by regressing against the percentage of UMIs originating from mitochondrial genes, S-phase and G_2–M-phase scores, and total read counts. A shared nearest neighbor graph was constructed based on the first 40 principal components computed from the scaled integrated data. Louvain clustering (63) was performed using the FindClusters() function at a resolution of 1.0 for major cell type identification. Clusters were annotated into major cell types by comparing markers with canonical markers for major populations: B cells (*Cd79a*, *Cd79b*, *Cd19*), T cells (*Cd3e*, *Cd3d*, *Cd8a*, *Cd4*), NK cells (*Klrb1c*, *Ncr1*, *Nkg7*), macrophages (*Cd68*, *Mrc1*, *C1qc*, *C1qb*), monocytes (*Lyz2*, *Vcan*, *Chil3*, *Fn1*), neutrophils (*S100a8*, *S100a9*, *Cxcl2*), cDC1 (*Xcl1*, *Cd36*, *Itgae*), cDC2 (*Itgax*, *H2-DMb1*, *Mgl2*), mregDC (*Fscn1*, Ccl22, *Cacnb3*), and pDC (*Siglech*, *Ccr9*, *Bsl2*).

Integration and Clustering Analysis of Neutrophils

Neutrophils identified above were integrated across samples for further analysis. Batch effects were removed by an anchor-based method (64) implemented in Seurat version 4.0 using the FindIntegrationAnchors and IntegrateData functions in Seurat with 8,000 "anchors" and the top 40 principal components. From the integrated data, scaled *z*-scores for each gene were calculated using ScaleData. A shared nearest neighbor graph was constructed based on the first 40 principal components, and Louvain clustering was performed using the RunUMAP and FindClusters functions at a resolution of 0.5. The FindAllMarkers function was used to identify cluster-specific neutrophil markers with logfc.threshold = 0.25 and test.use = "wilcox." Genes with Bonferroni-corrected *P* values <0.05 and an average log FC >0.25 were considered differentially expressed and visualized as a heatmap in Fig. 2C. To further assist the annotation of neutrophil clusters, we performed GSEA. Genes were ranked based on $-\log_{10}$ (*P* value)*(sign of $\log_2$FC) resulting from the FindAllMarkers function, with most upregulated genes at the top and most downregulated genes at the bottom. Preranked GSEA was performed on gene rankings using the R package fgsea (bioRxiv 2021:060012) with 10,000 permutations, against Hallmark, REACTOME, and GO databases from Molecular Signatures Database (MSigDB) (65–67). The normalized enrichment score (NES) of gene sets was visualized using heatmaps in Fig. 2D. Expression of glucose metabolism and hypoxia was calculated by the AddModuleScore function using gene sets "REACTOME_GLUCOSE_METABOLISM" and "HALLMARK_HYPOXIA," respectively, and visualized in Fig. 2E.

Survival Analysis

The N3 signatures were defined as genes exclusively expressed in N3 neutrophils and derived by comparing N3 cells with all $CD45^+$ cells, as well as with N1 and N2 neutrophils using FindMarkers. Genes with high $\log_2$FC, high percentage expression in N3, and low percentage expression in other cells were selected (Supplementary Table S3). Gene expression data (RSEM-derived transcripts per million values) and corresponding clinical information from TCGA were downloaded from the GDC data portal and cBioPortal. N3 signature scores in TCGA bulk tumors were calculated by simple-sample GSEA implemented in the GVSA (1.4.0) R package. Univariable Cox regression analysis was performed on OS. The resulting HRs were visualized in forest plots. For cancer types that exhibited significant associations

in the forest plot, we further generated Kaplan–Meier survival curves with the optimal cutoff of the N3 signature, which was determined using the surv_cutpoint function implemented in the survminer R package.

Bulk RNA-Seq Analysis

The raw RNA-seq reads were assessed for quality using FastQC (http://www.bioinformatics.babraham.ac.uk/projects/fastqc/). Quality trimming was performed using cutadapt (68) to remove reads with adaptor contaminants and low-quality bases. Read pairs with either end shorter than 25 bps were discarded from further analysis. The trimmed and filtered reads were then aligned to the mouse transcriptome (mm10) using STAR (61). Uniquely aligned reads were counted at the gene level using featureCounts (69) and then normalized using the DESeq2 package (70), taking into account RNA composition bias. Differential expression analysis between CD71$^+$ and CD71$^-$ samples was carried out using a negative binomial generalized linear model implemented in DESeq2, with multiple experimental factors accounted for. Genes with an FC >2 and an FDR-controlled P value < 0.05 were considered differentially expressed. For each analysis, genes were ranked by $-\log_{10}(P \text{ value})*(\text{sign of } \log_2 FC)$. The preranked gene list was used for preranked GSEA (version 4.0.2) to assess the enrichment of hallmarks, curated gene sets, and gene ontology terms in MSigDB (65, 66, 71). The resulting normalized enrichment scores and FDR-controlled P values were used to assess transcriptome changes. DEGs are available in Table 1.

Correlation In Vivo and In Vitro Neutrophils

First, we analyzed the bulk RNA-seq performed on *in vivo* neutrophils and identified a set of 606 genes (two-fold more than random) that were significantly differentially expressed in both *in vivo* and *in vitro* neutrophils (CD71$^+$ vs. CD71$^-$ neutrophils). To evaluate whether this observed overlap was greater than expected by chance, we performed a permutation test to calculate an empirical P value: (i) randomly selected A and B genes from the entire transcriptome 100,000,000 times, where A = the number of DEGs *in vivo* and B = the number of DEGs *in vitro*; (ii) for each permutation, determined C, the number of overlapping genes between A and B; and (iii) computed the empirical P value = the proportion of permutations, where C was greater than or equal to 606. A total of 3,494 DEGs in *in vivo* neutrophils were used to calculate the correlation between *in vivo* and *in vitro* samples. Briefly, the *in vivo* CD71$^+$ neutrophil signature was identified as significantly DEGs (3,494) in *in vivo* neutrophils (CD71$^+$ vs. CD71$^-$) from brain tumors. Mean $\log_2$-scaled expression values of the CD71$^+$ *in vivo* signature genes across biological replicates within the following groups were calculated: *in vitro* CD71$^+$ neutrophils, *in vitro* CD71$^-$ neutrophils, *in vivo* CD71$^+$ neutrophils, and *in vivo* CD71$^-$ neutrophils. Spearman correlation coefficients, computed using these mean expression values, were utilized to analyze the similarity between *in vitro* CD71$^+$ neutrophils and *in vivo* (brain tumor) CD71$^+$ neutrophils, as well as between *in vitro* CD71$^-$ neutrophils and *in vivo* CD71$^-$ neutrophils.

BrdU Staining

Mice were stereotactically injected with the SB28 cell line (10,000 cells/mouse). Fourteen days after the tumor cell injection, a one-time administration of BrdU was performed. The APC BrdU Flow Kit (BD Pharmingen, Cat#552598) was used, following the manufacturer's instructions. Briefly, 165 µL of BrdU solution (1.65 mg) were intraperitoneally injected into each mouse on day 0. Mice were euthanized 48, 96, 120, and 192 hours after BrdU injection (D0), and brain tumor tissues were collected and processed to obtain single-cell suspensions. Surface staining was first performed (30 minutes at RT). Cells were then washed, resuspended in 100 µL of BD Cytofix/CytoPerm Buffer, and incubated for 30 minutes on ice. Cells were washed with 1 mL of 1X BD Perm/Wash Buffer. Cells were then resuspended in 100 µL of BD CytoPerm Permeabilization Buffer and incubated for 10 minutes on ice, washed with 1X BD Perm/Wash Buffer, refixed for 5 minutes on ice with 100 µL of BD Cytofix/CytoPerm Buffer, and then washed with 1X BD Perm/Wash Buffer. Cells were then resuspended in 100 µL of diluted DNase (300 µg/mL in 1X PBS) and incubated for 1 hour at 37°C and then washed with 1X BD Perm/Wash Buffer. Cells were then stained with anti-BrdU (1:40) for 20 minutes at RT. Cells were finally acquired using a low/medium flow rate, no greater than 400 events/second. To study CD71$^-$ and CD71$^+$ survival within the tumor tissue, the peak of BrdU$^+$ cells (which happened at D4 after injection for both cell subsets) was set at 100%; starting from the peak, a mathematical model of nonlinear regression was applied to analyze the loss of BrdU$^+$ cells and calculate the half-life of neutrophils in GBM tissue (23).

Adoptive Transfers

Neutrophils were generated *in vitro* in normoxic or hypoxic conditions from naïve donor mice (CD45.2). At day 6, CD71$^-$ and CD71$^+$ neutrophils were FACS-sorted; 2.5×10^6 neutrophils per condition were injected in 100 µL of PBS (retro-orbitally) into recipient congenic mice (CD45.1). After 24 hours, blood, lungs, and spleens of recipient mice were collected, processed, and stained for FACS analysis. CountBright Absolute Counting Beads (Invitrogen, C36950) were used for absolute quantification of neutrophils. In another experimental setting, the SB28 cell line (1,000,000 cells in 200 µL of RPMI) was injected subcutaneously in naïve recipient mice (CD45.2). After 14 days, CD71$^-$ and CD71$^+$ neutrophils were FACS-sorted from the BM of congenic donor mice (CD45.1), mixed at a ratio of 1:1 (1×10^6 total neutrophils), and adoptively injected in 150 µL of PBS directly into the tumor of wild-type recipient mice. Seventy-two hours later, CD71$^-$ and CD71$^+$ neutrophils were FACS-sorted from the tumor and used to perform qRT-PCR (at least 1,000 cells per population were required). In some experiments, CD71$^-$ neutrophils were injected alone to check CD71 expression by FACS after 72 hours.

Generation of In Vitro Human Neutrophils

CD34$^+$ human stem cells were isolated from BM of donors and seeded in six-well plates in Iscove's modified Dulbecco's medium (IMDM, Gibco) supplemented with 20% FBS (Gibco) and 1% penicillin/streptomycin (Gibco), at a concentration of 60,000 cells/mL, 3 mL/well. G-CSF (PeproTech, 100 ng/mL) and GM-CSF (PeproTech, 25 ng/mL) were added on day 0 and every 3 days thereafter. At day 9, cells were transferred to the hypoxia chamber (1% O_2); in some conditions, GNE-140 was added at a concentration of 10 µmol/L on day 9 and 5 µmol/L every day until day 12. At day 13, CD71$^-$ and CD71$^+$ neutrophils were FACS-sorted and used to perform a suppression assay with T cells isolated from healthy donors. For ARG1 inhibition, norNOHA (Millipore, 750 µmol/L) was added during the suppression assay.

Immunofluorescence Staining and Analysis

SB28 brain tumors were embedded in Optimal cutting temperature compound (OCT) and frozen at −80°C. Ten-micrometer sections were cut from the OCT blocks and placed on slides to perform immunofluorescence staining. Briefly, sections were fixed with freshly made PFA 4% for 10 minutes at RT and washed and permeabilized for 20 minutes at RT with 1X PBS + 5% goat serum + 0.3% Triton X-100. Sections were washed and blocked for 1 hour at RT with 10% goat serum. Sections were then stained (in 1X PBS + 5% goat serum) with the following primary antibodies overnight at 4°C, in the dark, using a humid chamber: staining 1, anti-Ly6G rabbit (Cell Signaling Technology, 87048S) 1:20 + anti-CD71 rat (Proteintech, 65289-1-Ig) 1:50 and staining 2, anti-Ly6G rabbit 1:20 + anti-CD71 rat 1:50 + anti-CD3

AF647 (BioLegend, 100209) 1:20. Sections were washed and incubated with the following goat secondary antibodies for 2 hours at RT, in the dark, using a humid chamber: anti-rabbit AF555 (The Jackson Laboratory, 111-565-144) 1:500 + anti-rat AF750 (Abcam, AB175751) 1:300. Sections were then washed and, only for staining 1, were incubated again with the following primary antibodies for 2 hours at RT, in the dark, using a humid chamber: Anti-GLUT1 rabbit (Proteintech, 21829-1-AP) 1:250 + anti-CD73 rat (BioLegend, 127202) 1:20. Sections were washed and incubated with the following goat secondary antibodies for 2 hours at RT, in the dark, using a humid chamber: anti-rabbit AF647 (Invitrogen, A21244) 1:300 + anti-rat AF594 (BioLegend, 405422) 1:100. Sections were then washed, incubated for 5 minutes at RT with DAPI, and washed again. Coverslips were mounted using ProLong Diamond Antifade mounting media, left at 4°C for 24 hours, and then analyzed using Leica STELLARIS 8 3X TauSTED Super-Resolution. To analyze the distribution of neutrophil subsets in relation to $CD3^+$ T cells, $CD3^+$ T cells were identified in six different sections, from two different SB28 brain tumors. Neutrophil subsets were counted around $CD3^+$ T cells within a radius of 30 µm. To quantify $CD71^-$ and $CD71^+$ neutrophils in the hypoxic/glycolytic areas, hypoxic areas were defined as $CD73^{high}$, whereas glycolytic areas were defined as $GLUT1^{high}$. 4 hypoxic versus 4 non-hypoxic areas and 4 hypoxic glycolytic areas vs. 4 hypoxic non glycolytic areas were defined respectively in sections from 2 different tumors. The Nikon NIS-Elements Advanced Research (version 6.02.01) Build 1973 and the Bright Spot Detection tool were used to detect and count nuclei and objects per channel. CD71 and Ly6G channels were chosen as two single binary layers and were combined to create a third binary layer to identify double-positive cells. The auto measurement tool was then used to count the number of objects (single positives or double positives) per selected area. Cumulative counts were graphed.

Statistical Analysis

After testing for normal distribution of data, statistical analyses were performed using a two-tailed Student *t* test; a paired *t* test was used for matched samples; when more than two groups were compared, one- or two-way ANOVA with correction for multiple comparisons (Tukey or Holm–Šidák *post hoc* test) was used. Data were presented as mean ± SEM. The Pearson correlation coefficient with the associated two-tailed *P* value was calculated to study correlations. Kaplan–Meier plots were used for survival analysis, and the log-rank test was used to compare survival distributions between groups. A $P < 0.05$ was considered statistically significant.

Data Availability

Data from TCGA can be retrieved from their website. Bulk RNA-seq (GSE285509) and scRNA-seq (GSE285510) data are publicly available in the Gene Expression Omnibus.

Authors' Disclosures

M.A. Vogelbaum reports grants from the NIH during the conduct of the study as well as grants from Oncosynergy, Infuseon, DeNovo, and Carthera and personal fees from Servier, Biodexa, and Alexion outside the submitted work. J.R. Conejo-Garcia reports personal fees from Alloy Therapeutics and other support from Cellepus Therapeutics outside the submitted work and has a patent for Anixa Biosciences issued, licensed, and with royalties paid from the Wistar Institute and a patent for Compass Therapeutics pending to the Wistar Institute. No disclosures were reported by the other authors.

Authors' Contributions

A. Ugolini: Conceptualization, investigation, methodology, writing–original draft, writing–review and editing. **A. De Leo:** Conceptualization, investigation, methodology. **X. Yu:** Data curation, formal analysis, investigation. **F. Scirocchi:** Investigation, writing–original draft. **X. Liu:** Formal analysis. **B. Peixoto:** Investigation. **D. Scocozza:** Investigation. **A. Pace:** Investigation. **M. Perego:** Validation. **A. Gardini:** Investigation. **L. D'Angelo:** Investigation. **J.K.C. Liu:** Investigation. **A.B. Etame:** Investigation. **A. Rughetti:** Investigation. **M. Nuti:** Investigation. **A. Santoro:** Investigation. **M.A. Vogelbaum:** Investigation. **J.R. Conejo-Garcia:** Investigation. **P.C. Rodriguez:** Investigation. **F. Veglia:** Conceptualization, formal analysis, supervision, funding acquisition, validation, investigation, writing–original draft, project administration, writing–review and editing.

Acknowledgments

This work was supported by the Ben & Catherine Ivy Foundation Emerging Adult Glioma Award, the National Institute of Neurological Disorders and Stroke (R01 NS131912), and the American Cancer Society Institutional Research Grant (IRG-21-145-25). This was also supported in part by the Flow Cytometry Core Facility, the Molecular Genomics Core, the Proteomics & Metabolomics Core Facility, and the Biostatistics and Bioinformatics Shared Resource at the H. Lee Moffitt Cancer Center & Research Institute, a Comprehensive Cancer Center designated by the NCI and funded in part by Support Grant (P30-CA076292). This was also supported in part by the Wistar Institute's flow cytometry, genomics, histotechnology, and imaging facilities funded in part by Support Grant P30 CA010815. Analysis of human specimens from Sapienza (Italy) was in part supported by grant 2022M5LBKP PRIN 2022 and Sapienza RM1221816BCE0EAA (to A. Rughetti). A. Ugolini, A. Pace, and F. Scirocchi were students of the PhD program in Network Oncology and Precision Medicine at Sapienza University of Rome.

Note

Supplementary data for this article are available at Cancer Discovery Online (http://cancerdiscovery.aacrjournals.org/).

Received July 22, 2024; revised December 9, 2024; accepted February 26, 2025; posted first February 27, 2025.

REFERENCES

1. Jaillon S, Ponzetta A, Di Mitri D, Santoni A, Bonecchi R, Mantovani A. Neutrophil diversity and plasticity in tumour progression and therapy. Nat Rev Cancer 2020;20:485–503.
2. Hedrick CC, Malanchi I. Neutrophils in cancer: heterogeneous and multifaceted. Nat Rev Immunol 2022;22:173–87.
3. De Leo A, Ugolini A, Veglia F. Myeloid cells in glioblastoma microenvironment. Cells 2020;10:18.
4. Wang PF, Zhang YX, Su J, Yao K, Li SW, Huang GR, et al. Neutrophil depletion enhances the therapeutic effect of PD-1 antibody on glioma. Aging (Albany NY) 2020;12:15290–301.
5. Stupp R, Taillibert S, Kanner A, Read W, Steinberg D, Lhermitte B, et al. Effect of tumor-treating fields plus maintenance temozolomide vs maintenance temozolomide alone on survival in patients with glioblastoma: a randomized clinical trial. JAMA 2017;318:2306–16.
6. Sampson JH, Gunn MD, Fecci PE, Ashley DM. Brain immunology and immunotherapy in brain tumours. Nat Rev Cancer 2020;20:12–25.
7. Veglia F, Hashimoto A, Dweep H, Sanseviero E, De Leo A, Tcyganov E, et al. Analysis of classical neutrophils and polymorphonuclear myeloid-derived suppressor cells in cancer patients and tumor-bearing mice. J Exp Med 2021;218:e20201803.
8. Zilionis R, Engblom C, Pfirschke C, Savova V, Zemmour D, Saatcioglu HD, et al. Single-cell transcriptomics of human and mouse lung cancers reveals conserved myeloid populations across individuals and species. Immunity 2019;50:1317–34.e10.

9. Wu Y, Ma J, Yang X, Nan F, Zhang T, Ji S, et al. Neutrophil profiling illuminates anti-tumor antigen-presenting potency. Cell 2024;187:1422–39.e24.
10. Ng MSF, Kwok I, Tan L, Shi C, Cerezo-Wallis D, Tan Y, et al. Deterministic reprogramming of neutrophils within tumors. Science 2024;383:eadf6493.
11. Wang L, Liu Y, Dai Y, Tang X, Yin T, Wang C, et al. Single-cell RNA-seq analysis reveals BHLHE40-driven pro-tumour neutrophils with hyperactivated glycolysis in pancreatic tumour microenvironment. Gut 2023;72:958–71.
12. Maas RR, Soukup K, Fournier N, Massara M, Galland S, Kornete M, et al. The local microenvironment drives activation of neutrophils in human brain tumors. Cell 2023;186:4546–66.e27.
13. Rogers T, DeBerardinis RJ. Metabolic plasticity of neutrophils: relevance to pathogen responses and cancer. Trends Cancer 2021;7:700–13.
14. Veglia F, Sanseviero E, Gabrilovich DI. Myeloid-derived suppressor cells in the era of increasing myeloid cell diversity. Nat Rev Immunol 2021;21:485–98.
15. De Leo A, Ugolini A, Yu X, Scirocchi F, Scocozza D, Peixoto B, et al. Glucose-driven histone lactylation promotes the immunosuppressive activity of monocyte-derived macrophages in glioblastoma. Immunity 2024;57:1105–23.e8.
16. Genoud V, Marinari E, Nikolaev SI, Castle JC, Bukur V, Dietrich PY, et al. Responsiveness to anti-PD-1 and anti-CTLA-4 immune checkpoint blockade in SB28 and GL261 mouse glioma models. Oncoimmunology 2018;7:e1501137.
17. Boivin G, Faget J, Ancey PB, Gkasti A, Mussard J, Engblom C, et al. Durable and controlled depletion of neutrophils in mice. Nat Commun 2020;11:2762.
18. Condamine T, Dominguez GA, Youn JI, Kossenkov AV, Mony S, Alicea-Torres K, et al. Lectin-type oxidized LDL receptor-1 distinguishes population of human polymorphonuclear myeloid-derived suppressor cells in cancer patients. Sci Immunol 2016;1:aaf8943.
19. Watson MJ, Vignali PDA, Mullett SJ, Overacre-Delgoffe AE, Peralta RM, Grebinoski S, et al. Metabolic support of tumour-infiltrating regulatory T cells by lactic acid. Nature 2021;591:645–51.
20. Vignali PDA, DePeaux K, Watson MJ, Ye C, Ford BR, Lontos K, et al. Hypoxia drives CD39-dependent suppressor function in exhausted T cells to limit antitumor immunity. Nat Immunol 2023;24:267–79.
21. Dinh HQ, Eggert T, Meyer MA, Zhu YP, Olingy CE, Llewellyn R, et al. Coexpression of CD71 and CD117 identifies an early unipotent neutrophil progenitor population in human bone marrow. Immunity 2020;53:319–34.e6.
22. Aroca-Crevillén A, Vicanolo T, Ovadia S, Hidalgo A. Neutrophils in physiology and pathology. Annu Rev Pathol 2024;19:227–59.
23. Erben RG, Odörfer KI, Siebenhütter M, Weber K, Rohleder S. Histological assessment of cellular half-life in tissues in vivo. Histochem Cell Biol 2008;130:1041–6.
24. Ancey PB, Contat C, Boivin G, Sabatino S, Pascual J, Zangger N, et al. GLUT1 expression in tumor-associated neutrophils promotes lung cancer growth and resistance to radiotherapy. Cancer Res 2021;81:2345–57.
25. Si Y, Merz SF, Jansen P, Wang B, Bruderek K, Altenhoff P, et al. Multidimensional imaging provides evidence for down-regulation of T cell effector function by MDSC in human cancer tissue. Sci Immunol 2019;4:eaaw9159.
26. Evrard M, Kwok IWH, Chong SZ, Teng KWW, Becht E, Chen J, et al. Developmental analysis of bone marrow neutrophils reveals populations specialized in expansion, trafficking, and effector functions. Immunity 2018;48:364–79.e8.
27. Sippel TR, White J, Nag K, Tsvankin V, Klaassen M, Kleinschmidt-DeMasters BK, et al. Neutrophil degranulation and immunosuppression in patients with GBM: restoration of cellular immune function by targeting arginase I. Clin Cancer Res 2011;17:6992–7002.
28. Rodriguez PC, Quiceno DG, Zabaleta J, Ortiz B, Zea AH, Piazuelo MB, et al. Arginase I production in the tumor microenvironment by mature myeloid cells inhibits T-cell receptor expression and antigen-specific T-cell responses. Cancer Res 2004;64:5839–49.
29. Zhang D, Tang Z, Huang H, Zhou G, Cui C, Weng Y, et al. Metabolic regulation of gene expression by histone lactylation. Nature 2019;574:575–80.
30. Wang N, Wang W, Wang X, Mang G, Chen J, Yan X, et al. Histone lactylation boosts reparative gene activation post-myocardial infarction. Circ Res 2022;131:893–908.
31. Halestrap AP. The SLC16 gene family - structure, role and regulation in health and disease. Mol Aspects Med 2013;34:337–49.
32. Certo M, Llibre A, Lee W, Mauro C. Understanding lactate sensing and signalling. Trends Endocrinol Metab 2022;33:722–35.
33. Draoui N, Feron O. Lactate shuttles at a glance: from physiological paradigms to anti-cancer treatments. Dis Model Mech 2011;4:727–32.
34. Polański R, Hodgkinson CL, Fusi A, Nonaka D, Priest L, Kelly P, et al. Activity of the monocarboxylate transporter 1 inhibitor AZD3965 in small cell lung cancer. Clin Cancer Res 2014;20:926–37.
35. Bola BM, Chadwick AL, Michopoulos F, Blount KG, Telfer BA, Williams KJ, et al. Inhibition of monocarboxylate transporter-1 (MCT1) by AZD3965 enhances radiosensitivity by reducing lactate transport. Mol Cancer Ther 2014;13:2805–16.
36. Noe JT, Rendon BE, Geller AE, Conroy LR, Morrissey SM, Young LEA, et al. Lactate supports a metabolic-epigenetic link in macrophage polarization. Sci Adv 2021;7:eabi8602.
37. Wellen KE, Hatzivassiliou G, Sachdeva UM, Bui TV, Cross JR, Thompson CB. ATP-citrate lyase links cellular metabolism to histone acetylation. Science 2009;324:1076–80.
38. Sada N, Lee S, Katsu T, Otsuki T, Inoue T. Epilepsy treatment. Targeting LDH enzymes with a stiripentol analog to treat epilepsy. Science 2015;347:1362–7.
39. Guyon J, Fernandez-Moncada I, Larrieu CM, Bouchez CL, Pagano Zottola AC, Galvis J, et al. Lactate dehydrogenases promote glioblastoma growth and invasion via a metabolic symbiosis. EMBO Mol Med 2022;14:e15343.
40. Melero I, Sanmamed MF, Glez-Vaz J, Luri-Rey C, Wang J, Chen L. CD137 (4-1BB)-Based cancer immunotherapy on its 25th anniversary. Cancer Discov 2023;13:552–69.
41. Woroniecka KI, Rhodin KE, Dechant C, Cui X, Chongsathidkiet P, Wilkinson D, et al. 4-1BB agonism averts TIL exhaustion and licenses PD-1 blockade in glioblastoma and other intracranial cancers. Clin Cancer Res 2020;26:1349–58.
42. Ye Q, Song DG, Poussin M, Yamamoto T, Best A, Li C, et al. CD137 accurately identifies and enriches for naturally occurring tumor-reactive T cells in tumor. Clin Cancer Res 2014;20:44–55.
43. Ugolini A, Nuti M. CD137$^+$ T-cells: protagonists of the immunotherapy revolution. Cancers (Basel) 2021;13:456.
44. Ugolini A, Zizzari IG, Ceccarelli F, Botticelli A, Colasanti T, Strigari L, et al. IgM-Rheumatoid factor confers primary resistance to anti-PD-1 immunotherapies in NSCLC patients by reducing CD137$^+$ T-cells. EBioMedicine 2020;62:103098.
45. Zizzari IG, Di Filippo A, Botticelli A, Strigari L, Pernazza A, Rullo E, et al. Circulating CD137+ T cells correlate with improved response to anti-PD1 immunotherapy in patients with cancer. Clin Cancer Res 2022;28:1027–37.
46. Singhal S, Rao AS, Stadanlick J, Bruns K, Sullivan NT, Bermudez A, et al. Human tumor-associated macrophages and neutrophils regulate antitumor antibody efficacy through lethal and sublethal trogocytosis. Cancer Res 2024;84:1029–47.
47. Singhal S, Stadanlick J, Annunziata MJ, Rao AS, Bhojnagarwala PS, O'Brien S, et al. Human tumor-associated monocytes/macrophages and their regulation of T cell responses in early-stage lung cancer. Sci Transl Med 2019;11:eaat1500.
48. Gungabeesoon J, Gort-Freitas NA, Kiss M, Bolli E, Messemaker M, Siwicki M, et al. A neutrophil response linked to tumor control in immunotherapy. Cell 2023;186:1448–64.e20.
49. Veglia F, Perego M, Gabrilovich D. Myeloid-derived suppressor cells coming of age. Nat Immunol 2018;19:108–19.
50. van Vlerken-Ysla L, Tyurina YY, Kagan VE, Gabrilovich DI. Functional states of myeloid cells in cancer. Cancer Cell 2023;41:490–504.

51. Grover A, Sanseviero E, Timosenko E, Gabrilovich DI. Myeloid-derived suppressor cells: a propitious road to clinic. Cancer Discov 2021;11:2693–706.
52. Patel S, Fu S, Mastio J, Dominguez GA, Purohit A, Kossenkov A, et al. Unique pattern of neutrophil migration and function during tumor progression. Nat Immunol 2018;19:1236–47.
53. Peng Z, Liu C, Victor AR, Cao DY, Veiras LC, Bernstein EA, et al. Tumors exploit CXCR4^{hi} CD62L^{lo} aged neutrophils to facilitate metastatic spread. Oncoimmunology 2021;10:1870811.
54. Tulotta C, Stefanescu C, Chen Q, Torraca V, Meijer AH, Snaar-Jagalska BE. CXCR4 signaling regulates metastatic onset by controlling neutrophil motility and response to malignant cells. Sci Rep 2019;9:2399.
55. Casanova-Acebes M, Pitaval C, Weiss LA, Nombela-Arrieta C, Chèvre R, A-González N, et al. Rhythmic modulation of the hematopoietic niche through neutrophil clearance. Cell 2013;153:1025–35.
56. Adrover JM, Del Fresno C, Crainiciuc G, Cuartero MI, Casanova-Acebes M, Weiss LA, et al. A neutrophil timer coordinates immune defense and vascular protection. Immunity 2019;50:390–402.e10.
57. Ballesteros I, Rubio-Ponce A, Genua M, Lusito E, Kwok I, Fernández-Calvo G, et al. Co-Option of neutrophil fates by tissue environments. Cell 2020;183:1282–97.e18.
58. Salmaggi A, Gelati M, Pollo B, Marras C, Silvani A, Balestrini MR, et al. CXCL12 expression is predictive of a shorter time to tumor progression in low-grade glioma: a single-institution study in 50 patients. J Neurooncol 2005;74:287–93.
59. Bian XW, Yang SX, Chen JH, Ping YF, Zhou XD, Wang QL, et al. Preferential expression of chemokine receptor CXCR4 by highly malignant human gliomas and its association with poor patient survival. Neurosurgery 2007;61:570–8.
60. de Almeida Nagata DE, Chiang EY, Jhunjhunwala S, Caplazi P, Arumugam V, Modrusan Z, et al. Regulation of tumor-associated myeloid cell activity by CBP/EP300 bromodomain modulation of H3K27 acetylation. Cell Rep 2019;27:269–81.e4.
61. Dobin A, Davis CA, Schlesinger F, Drenkow J, Zaleski C, Jha S, et al. STAR: ultrafast universal RNA-seq aligner. Bioinformatics 2013;29:15–21.
62. Hao Y, Hao S, Andersen-Nissen E, Mauck WM 3rd, Zheng S, Butler A, et al. Integrated analysis of multimodal single-cell data. Cell 2021;184:3573–87.e29.
63. Blondel VD, Guillaume J-L, Lambiotte R, Lefebvre E. Fast unfolding of communities in large networks. J Stat Mech Theor Exp 2008;2008:P10008.
64. Stuart T, Butler A, Hoffman P, Hafemeister C, Papalexi E, Mauck WM 3rd, et al. Comprehensive integration of single-cell data. Cell 2019;177:1888–902.e21.
65. Subramanian A, Tamayo P, Mootha VK, Mukherjee S, Ebert BL, Gillette MA, et al. Gene set enrichment analysis: a knowledge-based approach for interpreting genome-wide expression profiles. Proc Natl Acad Sci U S A 2005;102:15545–50.
66. Liberzon A, Subramanian A, Pinchback R, Thorvaldsdóttir H, Tamayo P, Mesirov JP. Molecular signatures database (MSigDB) 3.0. Bioinformatics 2011;27:1739–40.
67. Liberzon A, Birger C, Thorvaldsdóttir H, Ghandi M, Mesirov JP, Tamayo P. The Molecular Signatures Database (MSigDB) hallmark gene set collection. Cell Syst 2015;1:417–25.
68. Kechin A, Boyarskikh U, Kel A, Filipenko M. cutPrimers: a new tool for accurate cutting of primers from reads of targeted next generation sequencing. J Comput Biol 2017;24:1138–43.
69. Liao Y, Smyth GK, Shi W. featureCounts: an efficient general purpose program for assigning sequence reads to genomic features. Bioinformatics 2014;30:923–30.
70. Love MI, Huber W, Anders S. Moderated estimation of fold change and dispersion for RNA-seq data with DESeq2. Genome Biol 2014;15:550.
71. Ashburner M, Ball CA, Blake JA, Botstein D, Butler H, Cherry JM, et al. Gene ontology: tool for the unification of biology. The Gene Ontology Consortium. Nat Genet 2000;25:25–9.